Journal of Wind Engineering & Industrial Aerodynamics 271 (2026) 106365

Contents lists available at ScienceDirect

Journal of Wind Engineering & Industrial Aerodynamics

journal homepage: www.elsevier.com/locate/jweia

Long-term wind-induced response of suspension bridges including static response, flutter stability, and parametric effects of turbulence

Niccolò Barni [a,*], Ole Øiseth [b], Øyvind Wiig Petersen [b], Claudio Mannini [a]

[a] Department of Civil and Environmental Engineering, University of Florence, Via S. Marta 3, Florence, 50139, Italy
[b] Department of Structural Engineering, Norwegian University of Science and Technology, Richard Birkelands vei 1A, Gløshaugen, Trondheim, 7034, Norway

ARTICLE INFO

Keywords:
Suspension bridges
Buffeting response
Extreme response
Long-term analysis
Parametric effects of turbulence

ABSTRACT

Parametric effects induced by atmospheric turbulence have emerged as an important factor influencing the aeroelastic behavior and extreme response of long-span suspension bridges. Originating from angle-of-attack fluctuations due to large-scale turbulence, these effects can significantly modify aerodynamic damping and stiffness, particularly for streamlined bridge decks. Long-term analysis, mainly adopted in the field of offshore structures, overcomes some limitations of classical Davenport theory-based approaches for calculating the dynamic response to turbulent wind of flexible structures, such as long-span suspension bridges. Among other aspects, it accounts for the influence of the statistical variability in turbulence parameters on the structural response, which is expected to impact on the actual role played by parametric effects of turbulence. However, accounting for these effects typically requires time-domain simulations, leading to prohibitive computational costs. This study introduces an efficient frequency-domain framework that incorporates the most significant parametric effect of turbulence (the so called "average parametric effect") into the long-term evaluation of extreme response. The proposed formulation also includes static response and flutter instability, two aspects usually overlooked in previous contributions. The methodology is applied to the Halsafjorden Bridge, a planned 2000-m span suspension bridge in Norway. Three different wind scenarios, in terms of turbulence intensity and mean wind speed, are also considered. Long-term extremes are close to the results of the classical short-term approach if the mean wind speed is the only environmental random variable. In contrast, non-negligibly larger long-term responses are obtained if the randomness in turbulence intensity is also considered. Moreover, results reveal that the parametric effects of turbulence can significantly increase the long-term extreme response, particularly in torsion, where turbulence-induced damping reductions may lead to response increments of up to 41% for a return period of 100 years. Their impact is greater than in classical short-term analyses, where the average parametric effect leads to an increase in the torsional response of about 33%. This behavior is even more pronounced for higher return periods. These findings highlight that the combined influence of parametric effects of turbulence and randomness in the environmental parameters (e.g., turbulence intensity) can properly be assessed only within a long-term analysis.

1. Introduction

Over the past decade, increasing attention has been devoted to the so-called parametric effects induced by atmospheric turbulence on the aeroelastic behavior of flexible civil structures, particularly long-span suspension bridges. These effects occur when large-scale turbulent fluctuations, especially in the direction traversal to mean wind direction and structural axis, alter the local angle of attack over time and thus affect the aerodynamic behavior of the structure. When self-excited forces exhibit strong sensitivity to the angle of attack, as is typically the case for streamlined bridge decks (e.g., Diana et al. 2013, Barni et al. 2021, Wu et al. 2020), variations in wind incidence can lead to significant changes in the effective stiffness and damping of the system. This effect gives rise to a class of time-variant dynamic systems commonly referred to as parametrically modulated, which may manifest as transient amplification of vibrations externally excited by turbulence (buffeting) (Barni et al., 2022; Calamelli et al., 2024) or even trigger aeroelastic instabilities such as random flutter (Bucher and Lin, 1988; Poirel and Price, 2003; Barni et al., 2024). The resulting modulation of self-excited forces has been modeled through various time-variant strategies (Lei et al., 2024), including rheological formulations (Diana et al., 2008, 2013; Diana and Omarini, 2020) and rational function approximations (Chen and Kareem, 2001, 2003; Barni et al., 2021, 2022), in which the

* Corresponding author.
E-mail address: niccolo.barni@unifi.it (N. Barni).

https://doi.org/10.1016/j.jweia.2026.106365
Received 23 September 2025; Received in revised form 12 December 2025; Accepted 23 January 2026
0167-6105/

aerodynamic coefficients evolve with the turbulence-induced angle of attack. These models show that fluctuations in wind incidence not only affect the quasi-steady aerodynamic terms but also modify the memory effects in the fluid–structure interaction. In contrast, it has been shown that the parametric effect associated with fluctuations in the wind velocity magnitude is marginal (Barni and Mannini, 2024). Among the nonlinear features that emerge, one of the most important, particularly in the context of wind-resistant design of long-span suspension bridges, is the change in the statistical distribution of response maxima. Indeed, parametric effects can significantly alter the effective damping and consequently the predicted response extremes, particularly as wind conditions approach the flutter instability threshold (Barni et al., 2022, 2024; Barni and Mannini, 2024).

The most widely adopted approach for estimating wind-induced extreme response remains the classical framework introduced by Davenport (Davenport, 1961, 1962), which combines Rice's formula for threshold crossing rates of Gaussian processes (Rice, 1944) with a Poisson model for maxima, and defines the peak response as proportional to the mean via the so-called gust response factor. This method is very convenient for design purposes, but, even renouncing to the simplification of the gust response factor and performing full dynamic calculations, this classical approach relies on several key assumptions that may not always hold, especially in the case of long-span bridges. Its main limitations are discussed here below.

1. Davenport's approach implicitly assumes that the extreme response associated with a given return period occurs at the corresponding design wind speed. However, such a maximum of the response can also be encountered for higher and lower mean wind speeds. Indeed, the pioneering work of Cook and Mayne (1980) (see also Cook and Mayne 1979, Kopp and Morrison 2018) showed that non-negligible underestimates of extremes may result from this simplified approach.
2. The method does not allow considering randomness in turbulence parameters (e.g., turbulence intensities), which is instead important especially (but not only) when a directional analysis is not possible, and which has been considered in some recent studies (Fenerci and Øiseth, 2017a,b; Castellon et al., 2022; Lystad et al., 2020). It has been shown that the peak response is more likely to result from a combination of moderately high values of the various random variables describing the wind event, rather than from the extreme of one of them (e.g., the design wind speed). Once again, ignoring this joint variability may lead to a non-conservative estimation of structural peak response.
3. It is assumed that the distribution of response maxima during a storm is sufficiently narrow for its expected value to be representative. However, this assumption may not hold for very flexible structures with low zero-upcrossing rates, as illustrated in Fig. 1. This issue is further exacerbated by the presence of uncertainties in wind and structural parameters, as pointed out by Solari (1997).
4. The use of a Poisson model for the distribution of maxima requires threshold crossings to be independent. In very flexible and lightly damped structures, such as long-span bridges, this condition may be violated due to the occurrence of clustered crossings, as discussed by Vanmarcke (Vanmarcke, 1975; Vanmarcke and Lai, 1980).
5. The peak factor in the classical approach is a function of the assumed duration of the design wind event. The sensitivity to such an "observation time" is more pronounced for flexible structures with low zero-upcrossing rates. In such cases, extending the observation time from 10 min to one hour can lead to differences in the estimated peak response of up to 20%–30%.

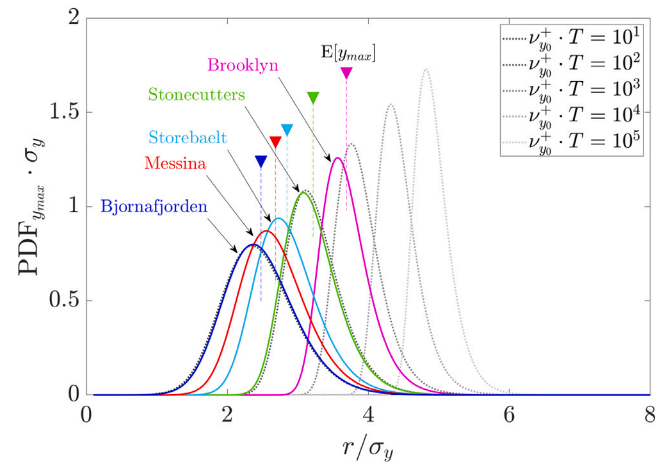

Fig. 1. Probability density function (PDF) of maxima for the lateral response of a few famous bridges (either existing or proposed), obtained for an observation time T of ten minutes (for the sake of simplicity, the zero-upcrossing rate $\nu_{y_0}^+$ is assumed to coincide with the first mode natural frequency). r represents the generic response threshold, and σ_y the response standard deviation.

Some of these limitations are well-established concepts in marine engineering (Kleiven and Haver, 2004; Haver and Kleiven, 2004) and have been addressed in offshore structure design standards (Norwegian Technology Standards Institution, 2007) through the adoption of full long-term extreme analysis. The full long-term approach (Næss, 1984; Næss and Moan, 2013) addresses the first two limitations mentioned above by integrating all extreme responses for a given observation time (short-term responses) across the full range of environmental conditions the structure may experience during its lifetime, weighted by their joint probability of occurrence. This inherently resolves the third issue, as the distribution of maximum response given a storm event with certain characteristics is directly included in the integration. Also, the dependence of the extreme response on the observation time (point 5.) is implicitly accounted for by a long term-analysis invoking the population probability distribution of the environmental parameters. Compared to most reliability approaches, which are based on the extreme value distribution of an intensity measure, this is also a great advantage when frequent events are important for the analysis (e.g., fatigue and vortex-induced vibrations). A few applications of long-term extreme analysis to suspension bridge response due to wind are already available in the literature (Lystad et al., 2021; Xu et al., 2022; Castellon et al., 2022; da Costa et al., 2023; Banday et al., 2025). In particular, Lystad et al. (2021) shows that long-term estimates can substantially differ from short-term predictions (up to 25% higher stresses).

Treating multiple turbulence parameters as random variables dramatically increases the computational cost, making brute-force evaluation of the long-term integral impractical for more than two/three variables, even in the frequency domain. In this context, the inclusion of parametric effects of turbulence becomes particularly critical. Indeed, their influence may be amplified within a long-term framework, where rare but highly turbulent wind conditions and high wind velocities are probabilistically considered. On the other hand, fully capturing them requires time-domain simulations for each short-term scenario (Chen and Kareem, 2003; Diana et al., 2013; Barni et al., 2022), compounding the computational burden and potentially rendering the analysis unfeasible. Therefore, reducing the computational cost is crucial, whether for analyzing nonlinear aeroelasticity (e.g., parametric effects of turbulence) or evaluating long-term extremes. For the second issue, one possible strategy is to reformulate the long-term extreme value integral, originally based on the conditional probability of short-term extremes (Borgman, 1973; Krogstad, 1985), as a structural reliability problem (Madsen et al., 2006; Melchers and Beck, 2018). This enables the use of inverse first- or second-order reliability methods (IFORM or ISORM), as demonstrated by Giske et al. (2017) and applied to wind turbines (Haver and Kleiven, 2004; Agarwal and Manuel, 2009) and bridges (e.g., Lystad et al. 2021, Quintela et al. 2025). An alternative strategy is the use of surrogate models, which can drastically reduce the number of required calculations. Among these, Gaussian Process Regression-based approaches (Rasmussen and Williams, 2005) have gained popularity thanks to recent advancements in machine learning (Hu and Mahadevan, 2016; Gaspar et al., 2014; Xiao et al., 2018), and have successfully been applied to long-term analysis of suspension bridges (Lystad et al., 2023; Castellon et al., 2023). In parallel, multiple timescale spectral analysis (Denoël, 2015), already applied to long-term response analysis (Fenerci et al., 2022), may allow for a more efficient computation of individual buffeting responses in the frequency domain.

This study aims to integrate the most significant parametric effects induced by atmospheric turbulence into the long-term extreme response analysis of a suspension bridge, within a numerically efficient frequency-domain framework designed to capture their impact on structural response. A second goal of this work is the integration of both static response and flutter instability into the long-term analysis. The former is typically evaluated separately at the design mean wind speed, and its rigorous incorporation into long-term analysis represents an important complication compared to offshore structures, as the static wind-induced response of suspension bridges, particularly in lateral bending, is usually large and cannot be ignored. On the other hand, instabilities such as flutter are usually neglected in long-term frameworks. Nevertheless, although flutter typically arises under rare environmental conditions, its large post-critical response can influence long-term extreme statistics.

The methodology is demonstrated using the Halsafjorden Bridge as a case study, considering three different wind scenarios. This is a 2000-m main span suspension bridge planned as part of Norway's E39 coastal highway project (Dunham, 2016). Owing to its exceptional flexibility and the associated low damping near the stability threshold, the validity of key assumptions commonly adopted in long-term analyses, such as the independent crossing hypothesis (point 4 in the previous list of classical Davenport approach limitations), is also critically assessed. Long-term results are compared to the outcomes of simplified short-term analyses, and the impact of parametric effects of turbulence is highlighted, providing new insight into their importance for an accurate and safe design of long-span suspension bridges.

2. Methodology

2.1. Short-term extremes

Let us assume the bridge response $R(t)$ is a stationary stochastic process over a short-term time period of length T, falling in the wind spectral gap (Van der Hoven, 1957). If high response level crossings can be considered statistically independent events (a reasonable assumption as long as the process is not excessively narrow-banded), the probability of not exceeding a threshold r within the specified time window of duration T (i.e., the probability that the maximum of $R(t)$ over this time window, indicated as $\hat{R}_{(T)}$, remains below r) can be calculated using a Poisson distribution (see, e.g., Næss and Moan 2013).

$$F_{\hat{R}(T)}(r) = \exp\left[-\nu_R^+(r) \cdot T\right] \tag{1}$$

where $\nu_R^+(r)$ denotes the mean upcrossing rate of threshold r. If the process is also Gaussian with non-zero mean μ_R, $\nu_R^+(r)$ can be expressed as:

$$\nu_R^+(r) = \nu_{R_0}^+ \exp\left[-\frac{1}{2}\frac{\left(r-\mu_R\right)^2}{m_{R_0}}\right] \tag{2}$$

where

$$\nu_{R_0}^+ = \frac{1}{2\pi}\sqrt{\frac{m_{R_2}}{m_{R_0}}}$$

and

$$m_{R_i} = \int_0^\infty \omega^i S_R(\omega)d\omega$$

provided that $r \geq \mu_R$; $\nu_{R_0}^+$ is the zero average upcrossing frequency. S_R is the power spectral density of the response, ω indicates a generic circular frequency, and m_{R_i} is the associated spectral moment of order i; in particular, m_{R_0} and m_{R_2} represent the variance of the response process and of its derivative, respectively.

If the sign of a specific response quantity is not of interest (e.g., for limit acceleration or deformation checks), one has to consider not only the upcrossing of barrier r but also the down-crossing of $-r$. This corresponds to consider upcrossings of threshold r by the process $|R(t)|$, known as D-type crossing (see, e.g., Vanmarcke 1975), as opposed to B-type crossing described above. In this case, the definition of the mean upcrossing rate becomes:

$$\begin{aligned}\nu_{|R|}^+(r) &= \nu_R^+(r) + \nu_R^-(-r)\\ &= 2\nu_{R_0}^+ \exp\left[-\frac{1}{2}\left(\frac{r^2+\mu_R^2}{m_{R_0}}\right)\right]\cosh\left(\frac{\mu_R \cdot r}{m_{R_0}}\right)\end{aligned} \tag{3}$$

where ν_R^+ and ν_R^- represent the rates of upcrossing the positive barrier r and down-crossing the negative barrier $-r$, respectively.

Under the above mentioned assumptions for the probability of first crossing of threshold r, in the classical Davenport approach, the peak dynamic response associated with a given return period T_{RP} can simply be calculated as the expected value of the distribution $\mathbb{E}\left[F_{\hat{R}(T)}(r)\right]$ under a mean wind speed with the same return period. The validity of the independent crossings assumption, which is instrumental in modeling maxima as a Poisson process (Eq. (1)), will be examined in Section 5.2 to assess whether it holds for the present case study.

2.2. Long-term extremes

In the long term, the bridge response induced by wind can no longer be considered stationary, as wind characteristics vary over the long-duration period T_{LT} (e.g., one year). Nevertheless, it is assumed that there exists a short-time window T (with $T_{LT} = N \cdot T$, where N is the number of short-term events composing the long-term interval), consistent with the wind spectral gap, such that the environmental parameters (e.g., mean wind velocity, turbulence intensity, and others) can be considered constant over it. As a result, the response process $R(t)$ can be assumed locally stationary within each short-term event. Then, the probability that the long-term extreme response $\hat{R}(T_{LT})$ does not exceed a certain threshold r can be written as:

$$P\left[\hat{R}(T_{LT}) \leq r\right] = P\left[\bigcap_{i=1}^{N} \hat{R}_i(T) \leq r\right] \tag{4}$$

If the short-term maxima $\hat{R}_i(T)$ from different intervals are assumed to be mutually independent (provided that $T \gg 2\pi\sqrt{m_{R_0}/m_{R_2}}$; see e.g., Krogstad 1985), the overall probability becomes a product of probabilities:

$$P\left[\bigcap_{i=1}^{N} \hat{R}_i(T) \leq r\right] = \prod_{i=1}^{N} P\left[\hat{R}_i(T) \leq r\right] \tag{5}$$

where each term $P\left[\hat{R}_i(T) \leq r\right]$ represents the probability that the maximum response in the ith short-term interval does not exceed r. According to the law of total probability, this can be expressed as:

$$P\left[\hat{R}_i(T) \leq r\right] = \int_{\mathbf{W}} F_{\hat{R}(T)}(r|\mathbf{w})\, f_{\mathbf{W}}(\mathbf{w})\, d\mathbf{w} \tag{6}$$

Here, $F_{\hat{R}(T)}(r \mid \mathbf{w})$ denotes the cumulative distribution function (CDF) of the maximum response over the short-term interval T, conditioned on a realization $\mathbf{w}$ of the environmental parameters, and $f_{\mathbf{W}}(\mathbf{w})$ is the probability density function (PDF) of those environmental parameters. The vector $\mathbf{w} \in \mathbf{W}$ represents a specific combination of environmental variables (e.g., mean wind speed, turbulence intensity, wind direction), and $\mathbf{W}$ denotes the domain of all possible realizations.

Assuming that the wind states are statistically independent and identically distributed events, meaning that the environmental vectors $\mathbf{w}$ associated with each short-term window are characterized by the same probability density function $f_{\mathbf{W}}(\mathbf{w})$, the product in Eq. (5) simplifies to the Nth power of a single probability $P\left[\hat{R}_i(T) \le r\right]$. Moreover, if threshold upcrossings are rare events and thus statistically independent within each short-term interval (Næss, 1984), the conditional distribution $F_{\hat{R}(T)}(r \mid \mathbf{w})$ can be approximated using a Poisson model. Under these assumptions, Eq. (4) becomes:

$$
\begin{aligned}
P\left[\hat{R}(T_{LT}) \le r\right] &= \left\{ \int_{\mathbf{W}} F_{\hat{R}(T)}(r|\mathbf{w}) f_{\mathbf{W}}(\mathbf{w})\, d\mathbf{w} \right\}^N \\
&= \left\{ \int_{\mathbf{W}} \exp\left[-\nu_R^+(r|\mathbf{w}) \cdot T\right] f_{\mathbf{W}}(\mathbf{w})\, d\mathbf{w} \right\}^N
\end{aligned}
\tag{7}
$$

where $\nu_R^+(r|\mathbf{w})$ is the mean rate of crossings the threshold r over the interval T, conditioned on the environmental parameters $\mathbf{w}$ (see Eq. (3)). It is important to note that raising the integral to a large power as N amplifies any approximation in the evaluation it. Accurate computation is therefore required, particularly in regions of the environmental parameter space $\mathbf{W}$ where the integrand attains its largest values. Accordingly, the discretization of $\mathbf{W}$ must be selected so as to guarantee an accurate numerical evaluation of the integral. However, if only rare events are of interest, $1 - P[\hat{R}_i(T) \le r]$ is a small quantity and then the following approximation holds:

$$
P\left[\hat{R}(T_{LT}) \le r\right] \simeq 1 - N \int_{\mathbf{W}} \left\{1 - \exp\left[-\nu_R^+(r|\mathbf{w}) \cdot T\right]\right\} f_{\mathbf{W}}(\mathbf{w})\, d\mathbf{w} \tag{8}
$$

This expression corresponds to the first-order expansion of $(1-x)^N \approx 1 - Nx$, which is valid for $Nx \ll 1$.

Several alternative approaches have been developed in the literature to estimate long-term response statistics. Among these, a methodology widely used in the field of marine structures is based on the assumption that extreme peaks are statistically independent but not identically distributed across all short-term conditions. In this context, the long-term distribution can be obtained either by determining the long-term average upcrossing rate, as suggested by Næss (1984), or by enforcing the ergodic mean (Borgman, 1973) of short term maxima, as done by Sagrilo et al. (2011) and Giske et al. (2017). In this work, we adopt the formulation of Eq. (7), as it allows for the inclusion of static response and flutter instability effects in the long-term evaluation without theoretical and practical issues, as will be discussed in Section 2.4. It is worth noting that Eq. (7) represents a structural reliability problem (Melchers and Beck, 2018) and can be solved using classical reliability methods such as IFORM or ISORM, as done in Sagrilo et al. (2011), Giske et al. (2017) and Lystad et al. (2021). Eq. (7) is similar to the equations of performance-based wind engineering (Ciampoli et al., 2011), adapted from the famous PEER equation in the field of earthquake engineering (Baker and Cornell, 2003), assuming the bridge response R as engineering demand parameter and the vector of environmental random variables $\mathbf{w}$ as intensity measure. Compared to these approaches, the major difference is that the probability density function of the whole population of the environmental random variables is invoked in Eq. (7) instead of the annual probability density function of the intensity measure.

2.3. Bridge response calculation

In this work, the wind-induced response of the bridge, expressed in terms of lateral, vertical and torsional deck displacements at a given spanwise position, is collected in a vector $\mathbf{R}(t) = [\, R_y(t)\;\; R_z(t)\;\; R_\theta(t)\,]^t$. Then, the vector $\boldsymbol{\mu}_R$ indicates the static (mean) response of the bridge. In the following, we restrict our attention to a single response component, so as not to overload the notation. The former is associated with the steady aerodynamic loading induced by the mean wind velocity V_m, and is computed here by projecting the mean aerodynamic force onto the modal shapes of the structure. The resulting modal loads are then solved in the modal space through the inversion of the modal structural stiffness matrix, and the results are subsequently projected back onto the physical coordinates to obtain the static displacements. Notably, this contribution depends only on the bridge stiffness, mean wind velocity, and aerodynamic coefficients of the deck section. It is also important to point out that the static rotation at mid-span, α_m, will be used later in Section 3 for evaluating the aerodynamic derivatives.

Buffeting analyses required to determine the spectral moments of the response are conducted using state-of-the-art multimodal buffeting approaches (Jain et al., 1996; Katsuchi et al., 1999; Chen et al., 2000; Øiseth et al., 2010), which account for aerodynamic damping and stiffness associated with self-excited forces arising from fluid–structure interaction. In short, buffeting response cross-spectral density $\mathbf{S}_R \in \mathbb{C}^{3\times3}$ is obtain by solving the following equation:

$$
\mathbf{S}_R(V_r, x, \omega) = \boldsymbol{\Phi}(x) \left[\mathbf{E}_{\boldsymbol{\eta}}^{-1}(V_r, \omega)\, \mathbf{S}_{\tilde{P}}(\omega)\, \mathbf{E}_{\boldsymbol{\eta}}^{-1*}(V_r, \omega)\right] \boldsymbol{\Phi}^t(x) \tag{9}
$$

where

$$
\begin{aligned}
\mathbf{E}_{\boldsymbol{\eta}}(V_r, \omega) = \Big[&-\tilde{\mathbf{M}}\omega^2 + \left(\tilde{\mathbf{C}}_0 - \tilde{\mathbf{C}}_{se}(V_r, \omega)\right) j\omega \\
&+ \left(\tilde{\mathbf{K}}_0 - \tilde{\mathbf{K}}_{se}(V_r, \omega)\right)\Big]
\end{aligned}
\tag{10}
$$

Here, $\boldsymbol{\Phi}(x) \in \mathbb{R}^{3\times N_m}$ is the matrix of mode shapes evaluated at the bridge deck position x (N_m is the number of modes considered), while $\mathbf{E}_{\eta}(\omega) \in \mathbb{C}^{N_m\times N_m}$ denotes the generalized impedance matrix in the frequency domain. The tilde symbol $(\tilde{\cdot})$ denotes quantities expressed in the modal coordinate system $\boldsymbol{\eta}$, while the asterisk $(^*)$ indicates the transpose conjugate of a matrix. Specifically, $\tilde{\mathbf{M}}$, $\tilde{\mathbf{C}}_0$, and $\tilde{\mathbf{K}}_0 \in \mathbb{R}^{N_m\times N_m}$ denote the structural mass, damping, and stiffness matrices, respectively, while $\tilde{\mathbf{C}}_{se}(\omega)$ and $\tilde{\mathbf{K}}_{se}(\omega) \in \mathbb{R}^{N_m\times N_m}$ are the aerodynamic damping and stiffness matrices, expressed as functions of the reduced velocity $V_r = V_m/(fB)$, where B is the bridge deck width and f the frequency of the motion (with $f = \omega/(2\pi)$). The imaginary unit is denoted by j. The generalized impedance matrix $\mathbf{E}_\eta(\omega)$ is also used to assess the aeroelastic stability of the system by inspecting its eigenvalues (see, e.g., Jain et al. 1996). The matrix $\mathbf{S}_{\tilde{P}}(\omega) \in \mathbb{C}^{N_m\times N_m}$ is the cross-spectral density matrix of the buffeting forces. Following the approach adopted by Øiseth et al. (2010), these forces are modeled using the linearized quasi-steady theory in combination with aerodynamic admittance functions, as follows:

$$
\mathbf{S}_{\tilde{P}}(\omega) = \int_\ell \int_\ell \boldsymbol{\Phi}^t(x_1)\mathbf{B}_q(\omega)\mathbf{S}_{\mathbf{v}}(\Delta x, \omega)\mathbf{B}_q^t(\omega)\boldsymbol{\Phi}(x_2)\, dx_1\, dx_2 \tag{11}
$$

where

$$
\mathbf{S}_{\mathbf{v}}(\Delta x, \omega) = \begin{bmatrix} S_{uu}(\Delta x, \omega) & S_{uw}(\Delta x, \omega) \\ S_{wu}(\Delta x, \omega) & S_{ww}(\Delta x, \omega) \end{bmatrix} \tag{12}
$$

$$
\mathbf{B}_q(\omega) = \frac{\rho V_m B}{2} \begin{bmatrix} 2\frac{D}{B}C_D & \frac{D}{B}C_D' - C_L \\ 2\,C_L & C_L' + \frac{D}{B}C_D \\ 2B\,C_M & B\,C_M' \end{bmatrix} \circ \mathbf{A}_{\mathbf{v}}(\omega) \tag{13}
$$

In Eqs. (11)–(13), $\Delta x = |x_1 - x_2|$ denotes the spanwise separation, and the double integral extends over the bridge span ℓ. The matrix $\mathbf{S}_{\mathbf{v}}(\Delta x, \omega)$ contains the auto- and cross-spectral densities of the longitudinal and vertical wind velocity fluctuations u and w, respectively (see, e.g., Eq. (21) in Section 4.3). The matrix $\mathbf{B}_q(\omega)$ is the buffeting load coefficient matrix, where ρ is the air density, B the deck width, and D the deck depth. C_D, C_L, and C_M denote the mean drag, lift, and moment static coefficients (assuming that drag is normalized based on the length D, while lift and moment are normalized based on B; see Section 4.2), while the prime indicates the derivative with respect to the angle of attack. The matrix $\mathbf{A}_\mathbf{v}(\omega)$ contains the aerodynamic admittance functions, which model the unsteadiness of buffeting forces. The symbol $(\circ)$ denotes the Hadamard (element-wise) product.

It is worth anticipating here that, if parametric effects induced by turbulence are considered, the impedance matrix $\mathbf{E}_\eta$ depends not only on the reduced velocity but also on the turbulent wind characteristics, especially the vertical turbulence intensity (see Section 3). Finally, the mean upcrossing rate $\nu_R^+(r)$ appearing in Eq. (2) can be calculated for every bridge response component from $\mathbf{S}_R(\omega)$ as explained in Section 2.1. The procedure for calculating the long-term extreme response is summarized in Appendix A.

2.4. Contribution of static response and flutter stability

In the case of suspension bridges, the mean static displacement induced by steady aerodynamic loads may be significant and can substantially influence the upcrossing rate of a given threshold (see Eq. (3)). Therefore, it is not justified to assume a purely dynamic formulation with zero mean response ($\mu_R = 0$), nor to evaluate the static response separately at the mean wind velocity associated with the selected return period T_{RP}, as the static and dynamic components nonlinearly interact in the long-term statistics. In this work, the static response is directly included in the mean upcrossing rate expression (Eq. (3)) and is incorporated in the long-term calculation without additional assumptions. However, there exist wind velocity range $V_m > V_m^*$ such that the mean response $\mu_R(V_m)$ exceeds the design threshold r, i.e., $r - \mu_R(V_m) < 0$. In this case, the static response alone leads to exceedance of the threshold r, and the conditional probability becomes null: $F_{\hat{R}(T)}(r|V_m) = 0$. In contrast, this line of reasoning cannot be extended to long-term formulations based on ergodic averages (e.g., Eq. (15) by Sagrilo et al. 2011, or Næss 1984 and Giske et al. 2017), which involve the logarithm of the conditional probability, $\log\left[F_{\hat{R}(T)}(r \mid V_m)\right]$. Indeed, when $V_m \to V_m^*$, $F_{\hat{R}(T)} \to 0$ and the logarithm tends to $-\infty$; therefore, these very rare events lead to a null long-term probability of non-exceedance. It is also important to remark that the proposed long-term formulation with the static response naturally converges to the static response caused by the mean wind speed associated with the same return period if the turbulence intensity tends to zero (i.e., if the dynamic contribution vanishes).

Flutter instability potentially leads to catastrophic oscillations of a bridge; therefore, design criteria usually require that the flutter critical wind speed is higher than a design wind speed associated with a return period significantly larger than that considered for buffeting loads. As a result, the combinations of environmental parameters $\mathbf{w}$ that trigger flutter (i.e., that make the real part of the eigenvalues of the impedance matrix in Eq. (10) positive at the flutter frequency) define a sub-domain $\mathbf{W}_f \subset \mathbf{W}$, which is generally associated with very low probability. Nevertheless, the contribution of this unstable domain to the long-term integral in Eq. (7) might not be negligible if the annual flutter probability (namely, $1-\left(1-\left\{\int_{\mathbf{W}_f} f_\mathbf{W}(\mathbf{w})\,d\mathbf{w}\right\}\right)^N$) is not vanishingly small. Rigorously accounting for the impact of flutter on long-term response would require modeling the post-critical behavior via nonlinear formulations that include large structural displacements (e.g., Salvatori and Spinelli 2006) and nonlinear self-excited forces (e.g., Gao et al. 2024, Wu et al. 2023). Nowadays, this is still very challenging from the modeling point view, computationally expensive, and also very uncertain since the amplitudes of limit-cycle oscillations are highly sensitive to nonlinear structural damping (in addition to aerodynamic damping, obviously). This is also the reason why flutter instability has never been considered in long-term extreme response evaluations (Castellon et al., 2023; Lystad et al., 2023).

In a reasonably simplified way, we assume here a linear behavior of the system (i.e., the divergence of the oscillations beyond the critical wind speed), implying that the probability that the response remains below a threshold r is null ($F_{\hat{R}(T)}(r|\mathbf{w}) = 0$ for every $\mathbf{w} \in \mathbf{W}_f$) for any r of practical interest and for every point along the bridge span. Naturally, this approach has some limitations, as illustrated in Fig. 2. In particular, it may become overconservative when the threshold associated with the target return period falls within the range of limit-cycle oscillation amplitudes that occur after the onset of flutter and can be not so large in some cases (the r-threshold domain highlighted in red in Fig. 2). However, such scenarios are considered unrealistic for streamlined bridge cross-sections, where vibrations typically grow rapidly once instability sets in, as confirmed by experiments on flat plates (Pigolotti et al., 2017) and full bridge models (Xu et al., 2021). Therefore, the practical impact of this limitation is negligible for the class of structures considered here. The proposed approach provides a reasonable penalization of long-term response contributions from the critical environmental sub-domain $\mathbf{W}_f$, under the idealized assumption of indefinitely linear post-critical behavior, an approximation conceptually analogous to the assumption of indefinitely linear material behavior in structural analysis. In this sense, the approach can be regarded as conservative to a large extent.

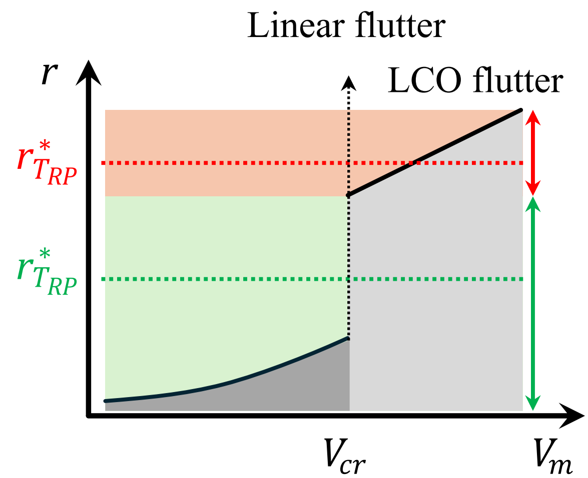

Fig. 2. Schematic representation of the bridge pre- and post-critical buffeting response. The two scenarios of extreme bridge response at a specific return period ($r_{T_{RP}}$), corresponding to amplitudes within and beyond the jump associated with the subcritical bifurcation, are shown in green and red on the ordinate, respectively.

3. Average parametric effect

Over the past thirty years, models have been developed to capture the impact of turbulence-induced angle-of-attack variations on unsteady self-excited forces (Chen and Kareem, 2003; Diana et al., 2013; Barni et al., 2022). The physical concept behind these models is that the large scales of turbulent wind (low-frequency part of the turbulence spectrum) slowly vary the wind inclination seen by the bridge cross section. Such variations in the angle of attack can be very pronounced (much higher than those induced by bridge motion; see, e.g., Barni et al. 2021, Bocciolone et al. 1992 and Diana et al. 1993) and instantaneously change along the bridge span according to the spanwise correlation of turbulence. When bridge aerodynamic derivatives are sensitive to variations in the angle of attack, as shown for many bridge cross sections (e.g., Barni et al. 2021, Diana et al. 2013, Diana and Omarini 2020, Argentini et al. 2016), stochastic changes in aerodynamic damping and stiffness occur over time. Recent studies (Barni and Mannini, 2024; Barni et al., 2024) have demonstrated that, during a synoptic wind event, turbulence-induced parametric effects can destabilize structures like the Hardanger Bridge, Norway, primarily through the so-called "average parametric effect", which arises from the difference between the average aerodynamic derivatives over a fluctuating angle of attack and those calculated for the average angle of attack, α_m (Barni and Mannini, 2024) (α_m is the sum of the bridge static rotation under wind, θ_{st}, and the mean wind-velocity inclination, α_W). This effect depends on the probability density function of the angle of attack, $\alpha(t) = \text{atan}[w(t)/(V_m + u(t))]$, where u and w are the longitudinal and vertical turbulent components of the wind velocity, and V_m is the mean wind speed, neglecting the contribution of bridge motion. It is worth noting that the average parametric effect depends solely on one-point statistics of turbulence, meaning that it is not influenced by the spanwise correlation of wind velocity fluctuations (Barni and Mannini, 2024).

To account for the average parametric effect of turbulence in a frequency-domain buffeting calculation, one can consider an average set of aerodynamic derivatives, $\overline{AD}$, determined through the following ensemble average:

$$\overline{AD}\left(V_r, \alpha_m\right) = \text{E}[AD(V_r, \alpha_m)] = \int AD(V_r, \alpha)\, f_\alpha(\alpha, \alpha_m)\, d\alpha \tag{14}$$

where $AD(V_r, \alpha)$ represents a generic aerodynamic derivatives, provided by either the 2D Rational Function Approximation (2D RFA) model (Barni et al., 2021) or other approximations or interpolations in the multivariate domain of reduced velocity V_r and angle of attack α. Here, $f_\alpha(\alpha, \alpha_m)$ is the probability density function of the angle of attack, and α_m represents the sum of mean wind inclination and bridge steady rotation under mean wind. Assuming that the probability distribution of the angle of attack coincides with that of vertical turbulence (i.e., $\alpha = \text{atan}[w/(V_m + u)] \approx w/V_m$) and that the latter is Gaussian, the PDF of the angle of attack has mean α_m and standard deviation I_w (Barni and Mannini, 2024), where the latter denotes the vertical turbulence intensity:

$$f_\alpha(\alpha, \alpha_m) = \frac{1}{I_w\sqrt{2\pi}} \exp\left[-\frac{1}{2}\left(\frac{\alpha - \alpha_m}{I_w}\right)^2\right] \tag{15}$$

The major simplification in this approach is that all turbulent fluctuations are considered effective for the average parametric effect. Indeed, a well-known open issue is associated with the turbulence spectrum cut-off for parametric excitation. The current method is supposed to overestimate slightly the average parametric effect of turbulence, and this should be borne in mind for design purposes (especially when parametric effects reduce the impact of the wind load). However, the effect of introducing a cut-off in the parametric excitation bandwidth has been analyzed and quantified in detail for another bridge in Barni and Mannini (2024), where excluding the higher-frequency part of the spectrum was shown to produce only limited changes in the predicted response. It is also important to stress that the average parametric effect as calculated in Eq. (14) does not require a Gaussian probability density function for the angle of attack. Non-Gaussian models for the turbulent velocities (e.g., for the vertical component, which is often observed to exhibit marked non-Gaussian features; see e.g., Liu et al. 2011 and Buono et al. 2024) could in principle be used in Eq. (14) by replacing the Gaussian probability density function in Eq. (15), or a time-domain procedure could be followed if wind velocity time histories are available or simulated beforehand. Therefore, Gaussianity is a convenient baseline rather than a fundamental requirement for estimating the average parametric effect. By contrast, introducing non-Gaussian turbulence at the short-term response level would make Rice's formula for the upcrossing rates (Eqs. (2)–(3)) no longer valid, and would require a different first-passage framework for short-term extremes, which is beyond the scope of the present work.

4. Case study

4.1. Halsafjorden bridge

Halsafjord, a fjord approximately 2100 m wide and 490 m deep, is concerned by Norway's Ferry-Free E-39 project. Among the proposed designs for crossing the fjord (e.g., the two-span suspension bridge with tension-leg-platform floating pylons proposed in Aas-Jakobsen et al. (2023)), the full-span suspension bridge with a main span of 2000 m has been selected for this study. The bridge features two 300 m-tall reinforced concrete towers, a sag-to-length ratio of the main cables of 8.8, and a deck supported by 83 hangers on each side, spaced 24 m apart. The deck, with a mid-span elevation of 65 m, comprises two steel box girders, each 2.5 m high and 16.5 m wide, spaced 4 m apart, while the main cables are spaced 36 m apart (see Fig. 3). To enhance stability, a central buckle at mid-span restricts relative displacements in the bridge axis direction between the main cables and the stiffening girder, effectively increasing the stiffness associated with all antisymmetric modes.

The bridge modal properties are obtained using a finite element model developed in Abaqus© (Fig. 4). Main and side suspension cables and all hangers are modeled with truss elements (cables: area A = 0.45 m^2, Young's modulus E = 200 GPa; hangers: $A = 4 \times 10^{-3}$ m^2, E = 160 GPa; the density is 7850 kg/m^3). The deck is modeled with a spine beam approach. In particular, each steel box girder is represented by a Timoshenko beam with $A = 0.73$ m^2, second moments $I_y = 0.64$ m^4 and $I_z = 17.14$ m^4, torsional constant $J = 1.85$ m^4, mass per unit length $m = 9300$ kg/m, and rotary inertia per unit length $I_r = 1.2 \times 10^6$ kg m^2/m. The reinforced-concrete towers are modeled as beam elements with equivalent sectional properties varying along the height, with E = 35 GPa and density 2500 kg/m^3, laterally linked by cross-beams at elevations 50, 120, 200 and 290 m. The tower bases are clamped to the foundations; the mid-span buckle is implemented as a longitudinal constraint between the main cables and the stiffening girders. The finite element model includes geometric nonlinearities of the cables during the application of dead loads. A modal analysis of the structure is conducted based on the tangent stiffness matrix corresponding to the deformed configuration under dead load. The first 100 modes are extracted, covering a frequency range from 0.042 Hz to 0.98 Hz. Structural damping is modeled as proportional modal damping, with a constant ratio of ζ = 0.005. The key modes for buffeting and flutter analyses are illustrated in Fig. 5.

4.2. Aerodynamic coefficients

To compute the bridge buffeting response, it is necessary to determine both the static coefficients and the aerodynamic derivatives of the Halsafjorden Bridge cross-section. These crucial coefficients are obtained through wind tunnel tests conducted at the Fluid Mechanics Laboratory of the Norwegian University of Science and Technology in Trondheim, Norway. A 1:50 sectional model of the bridge deck was used in the tests, incorporating all non-structural details, such as barriers and aerodynamic appendices. The experimental setup and the static and aeroelastic test procedure employed are described in Barni et al. (2021). The static coefficients are measured over a range of angles of attack between −10° and +10°, as shown in Fig. 6. These coefficients are used to define the matrix $\mathbf{B}_q$, reported here in numerical form as it will be useful later for further considerations:

$$\mathbf{B}_q(\omega) = \frac{\rho V_m B}{2}\begin{bmatrix} 0.165 & 0.224 \\ -0.406 & 2.491 \\ -1.323 & 22.365 \end{bmatrix} \circ \mathbf{A}_\mathbf{v}(\omega) \tag{16}$$

Since specific admittance functions for the Halsafjorden Bridge are not available, Davenport's formulation (Davenport, 1962) is used for all aerodynamic admittance functions in $\mathbf{A}_\mathbf{v}(\omega)$.

Aerodynamic derivatives are measured at 13 discrete mean angles of attack, spanning from −8° to +8° (namely, [−8, −5, −4, −3, −2, 0, 2, 3, 4, 5, 6, 7, 8]°). This range ensures a satisfactory representation of their dependency on the angle of attack, which is specifically needed to compute the average aerodynamic coefficients as described in Eq. (14) in Section 3. Reduced velocities V_r up to 25 are considered. A selection of aerodynamic derivatives is presented in Fig. 7 for a

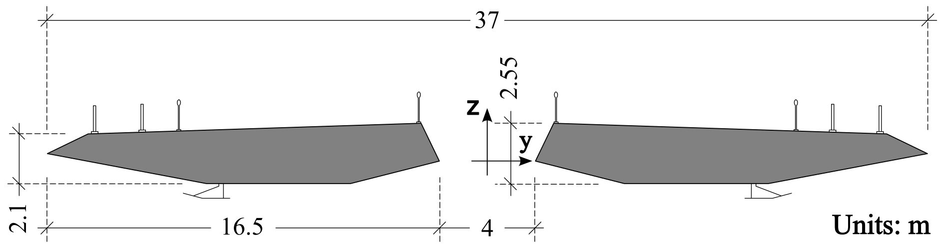

Fig. 3. Sketch of the Halsafjorden Bridge twin-deck cross-section.

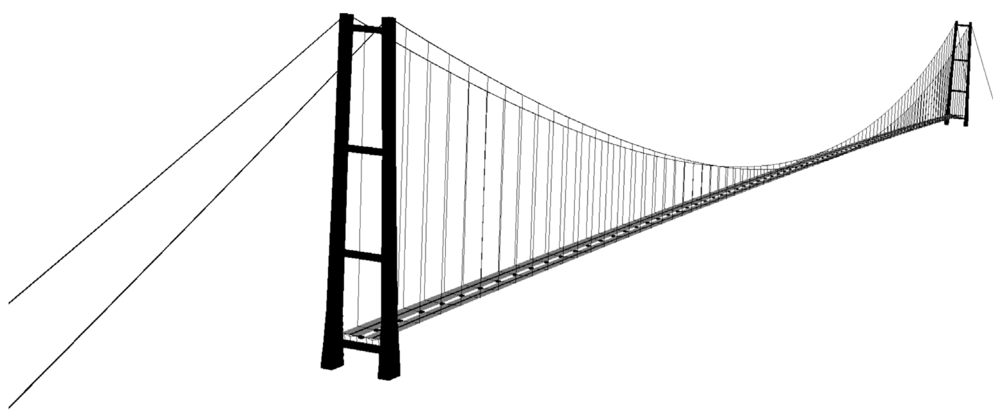

Fig. 4. Perspective view of the Halsafjorden Bridge finite-element model.

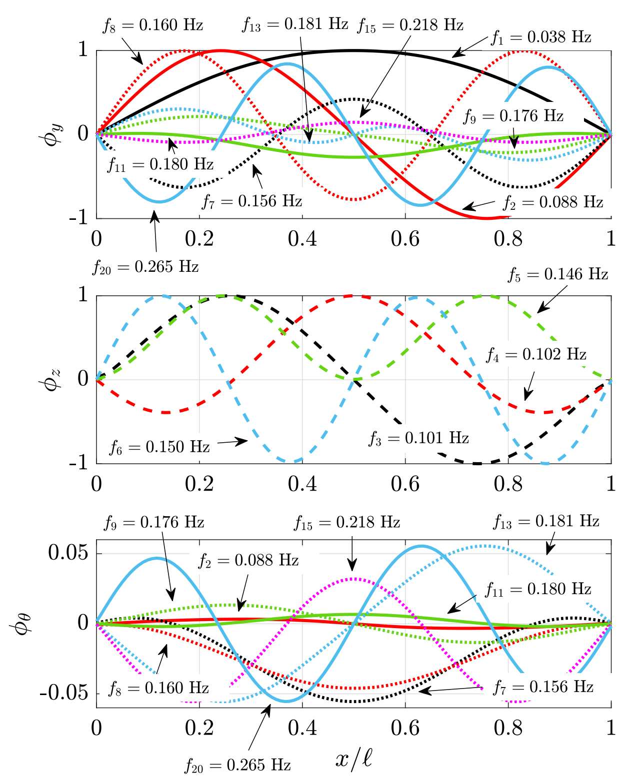

Fig. 5. Shapes and frequencies of the most important modes used in the buffeting and flutter analyses. ℓ denotes the bridge main span.

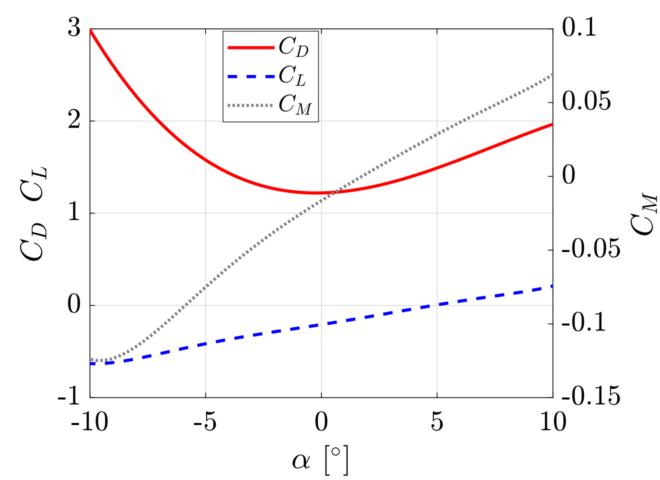

Fig. 6. Static aerodynamic coefficients for the Halsafjorden Bridge deck section. C_D is normalized based on the deck depth D, while C_L and C_M based on the width B.

subset of angles of attack. The 2D RFA model approximation is used to derive the functions $AD(V_r, \alpha)$ in Eq. (14). For values of α outside the available range, the aerodynamic coefficients are assumed equal to their values at −8° and +8°. It is apparent that the aerodynamic derivatives are highly sensitive to variations in the angle of attack. In particular, the aerodynamic derivative P_1^*, which contributes directly to the aerodynamic damping in the lateral motion, generally decreases as the angle of attack varies (the aerodynamic damping increases), for both positive and negative values. Similarly, the key aerodynamic coefficient A_2^*, which provides a direct contribution to torsional aerodynamic damping, becomes positive (negative aerodynamic damping) for angles of attack lower than approximately lower than −4° (nose-down). This, joined to the fact that such aerodynamic derivatives have a nonlinear and non-antisymmetric pattern with respect to almost every angle of attack, makes P_1^* and A_2^* coefficients sensitive to the average parametric effect of turbulence (Barni and Mannini, 2024). In particular, vertical turbulence intensities of 5.6% and 8.3% increase the lateral aerodynamic damping by approximately 9% and 16%, and

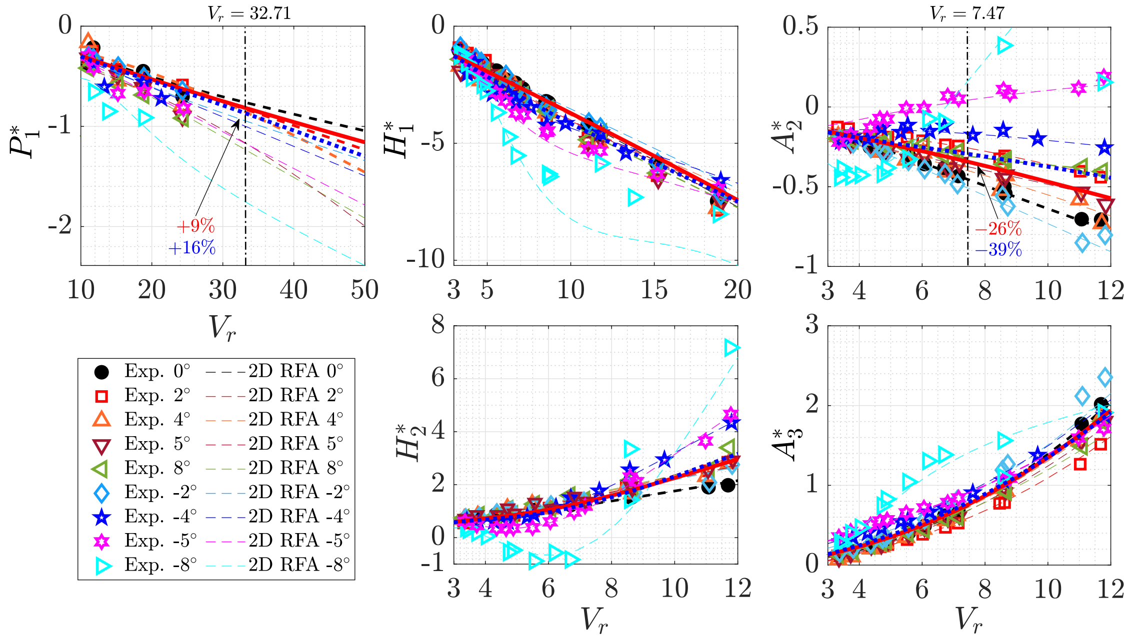

Fig. 7. Selection of aerodynamic derivatives for the Halsafjorden Bridge. The background dashed lines represent the 2D RFA approximations. Coefficients measured at various mean angles of attack are compared with those averaged around $\alpha_m = 0°$ (Eq. (14)), indicated with a thick red and a dotted blue line for vertical turbulence intensities $I_w = 5.6\%$ and 8.3%, respectively. The reduced-velocity range relevant for buffeting is considered. The dash-dotted vertical lines at $V_r = 32.71$ and 7.47 indicate the reduced velocities associated with the 100-years return period mean wind speed and the first symmetric lateral and torsional modes, respectively. At high V_r, P_1^* is extrapolated using the quasi-steady relation $P_1^* = -C_D V_r/\pi$.

reduces torsional aerodynamic damping by approximately 26% and 39%, respectively, for a mean wind speed of 46.1 m/s (see the next section). As for the direct contribution to the vertical aerodynamic damping, represented by H_1^*, the averaged coefficients do not vary significantly for these values of vertical turbulence intensity. A similar behavior is observed for the coefficient A_3^*, which accounts for the primary contribution to aerodynamic stiffness in torsion and is responsible for the reduction in the frequency of the bridge torsional modes. In contrast, the average parametric effect can lead to significant variations in other aerodynamic derivatives, such as H_2^*, which contributes to vertical aerodynamic damping due to the torsional motion and can non-negligibly affect the flutter critical velocity. It is also worth noting that the static moment coefficient is slightly negative at zero angle of attack, which is uncommon for a twin-deck bridge section. This leads to a negative (nose-down) static rotation of the deck, which shifts the bridge's steady angle of attack (θ_{st}), potentially exacerbating the parametric effect of turbulence.

4.3. Wind model

A long-term analysis requires a probabilistic description of environmental variables. In this work, the probabilistic wind model originally developed for the Sulafjorden site (Castellon et al., 2022), Norway, is slightly revised to serve as the baseline wind scenario. Given the geographical similarity between Sulafjord and Halsafjord, the model is considered representative of the wind environment at the bridge site. For details on data acquisition and processing, the Reader can refer to Castellon et al. (2022).

The model defines a joint probability distribution over a vector of environmental parameters $\mathbf{w}$, which is factorized as:

$$f_{\mathbf{w}}(\mathbf{w}) = f_{\mathbf{w}_t}(\mathbf{w}_t|V_m) f_{V_m}(V_m), \quad \mathbf{w}_t = \mathbf{w} \setminus V_m \tag{17}$$

where f_{V_m} is a lognormal distribution characterizing the mean wind velocity (with parameters μ and σ):

$$f_{V_m} = \frac{1}{\sqrt{2\pi}\sigma V_m} \exp\left[-\frac{\left(\log(V_m) - \mu\right)^2}{2\sigma^2}\right] \tag{18}$$

Table 1
Summary of environmental parameters in the various long-term response analyses. "r.v." stands for random variable. Mean (denoted here as δ_u and δ_w) and standard deviation of the turbulence intensities are provided in Fig. 9 as a function of the mean wind velocity V_m.

Long-term analyses	V_m	I_u	I_w	others
$\mathbf{w} = V_m$	r.v.	$\delta_u(V_m)$	$\delta_w(V_m)$	constant
$\mathbf{w} = [V_m\ I_w]^t$	r.v.	$I_w \frac{\delta_u(V_m)}{\delta_w(V_m)}$	r.v.	constant
$\mathbf{w} = [V_m\ I_u\ I_w]^t$	r.v.	r.v.	r.v.	constant

and $f_{\mathbf{w}_t}$ is a multivariate lognormal distribution with $n = \dim(\mathbf{w}_t)$ components:

$$f_{\mathbf{w}_t} = (2\pi)^{-\frac{n}{2}} (\det \boldsymbol{\Sigma}_t)^{-\frac{1}{2}} \prod_{i=1}^{n} w_{t,i}^{-1} \times \exp\left[-\frac{1}{2}\left(\log(\mathbf{w}_t) - \boldsymbol{\mu}_t\right)^{\top} \boldsymbol{\Sigma}_t^{-1} \left(\log(\mathbf{w}_t) - \boldsymbol{\mu}_t\right)\right] \tag{19}$$

The vector $\mathbf{w}_t = \mathbf{w} \setminus V_m$ denotes the subset of environmental random variables excluding the mean wind velocity V_m, collecting turbulence random environmental parameters. The conditional distribution $f_{\mathbf{w}_t}(\mathbf{w}_t|V_m)$ is modeled as a multivariate lognormal distribution, where $\boldsymbol{\mu}_t$ and $\boldsymbol{\Sigma}_t$ are the mean vector and covariance matrix of $\log(\mathbf{w}_t)$, respectively, both depending on the mean wind velocity.

In this work, the long-term response analysis is first carried out considering only V_m as a random variable (deterministic turbulence case), to allow a direct comparison between the long-term approach and the classical Davenport short-term response calculation. Subsequently, the vertical turbulence intensity I_w is introduced as a second random variable, so that the turbulent environmental vector becomes $\mathbf{w}_t = I_w$. In this case, however, the value of I_u still varies in the long term analysis and is determined from I_w based on the ratio between their mean values in the probabilistic model (Table 1). This is equivalent to treating I_u conditioned on V_m as a random variable perfectly correlated to the corresponding I_w, having a lognormal distribution with the mean equal to the expected value of I_u and the same coefficient of variation as

Table 2
Mean wind speed ($\hat{V}_m^{100\,\mathrm{yrs}}$ denotes the 100-years return-period mean wind speed) and turbulence intensities used for the classical short-term analysis. Moreover, the parameters of the lognormal distribution of V_m (μ and σ) are also reported.

Wind scenarios	V_m			I_u [%]	I_w [%]
	$\hat{V}_m^{100\,\mathrm{yrs}}$ [m/s]	μ	σ		
A	46.1	1.059	0.546	8.8	5.6
B	46.1	1.059	0.546	13.3	8.3
C	52.1	1.182	0.546	13.3	8.3

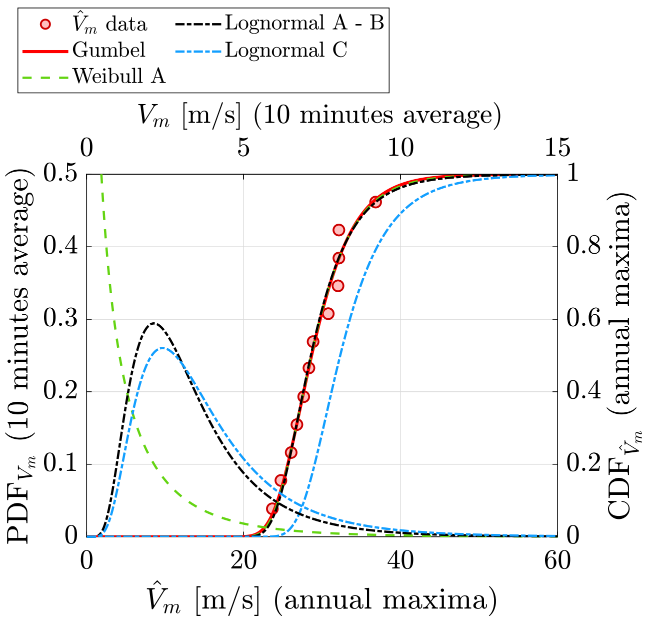

Fig. 8. Cumulative distribution functions (CDFs) of annual maximum mean wind velocity V_m for wind scenarios A, B and C along with the plotting position of measured data. The associated probability density functions (PDFs) of mean wind velocity population V_m are also shown. Weibull and Weibull^N probability distributions used in Castellon et al. (2022) are also reported for the sake of comparison.

I_w. Finally, a third set of analyses are carried out properly considering I_u as a conditioned random variable ($\mathbf{w}_t = [I_u\, I_w]^t$) according to the reference probabilistic wind model in Castellon et al. (2022). Clearly, introducing wind direction as an additional random variable would reduce the variability in these parameters. However, this approach is often impractical in long-term evaluations due to the high computational cost and the limited availability of directional wind data. All the remaining turbulent wind parameters are assumed to be deterministic and are defined as described at the end of this section.

Due to the limited availability of wind data (approximately 20 years, partly measured and partly derived from hindcast simulations, see Ágústsson et al. 2024), the probabilistic model for the ten-minutes mean wind velocity V_m is constructed to prioritize an accurate representation of extreme events, as these are expected to contribute most significantly to long-term response extremes. However, since even non-extreme wind conditions may influence the long-term response due to their higher probability of occurrence, the model should also reasonably reflect the overall distribution of the population. According to the asymptotic theorem of extreme value statistics (Gumbel, 1958), the Gumbel distribution representing the annual maximum mean wind speed $\hat{V}_m$ can be interpreted as the maximum of N independent random variables (where $N = 52596$ is again the number of short-term events in a year), all with the lognormal distribution of the mean wind speed population. Consequently, the annual non-exceedance probability equals the product of the non-exceedance probabilities over each short-term event throughout the year:

$$F_{\hat{V}_m}(V_m) = \left[F_{V_m}(V_m)\right]^N \tag{20}$$

where $F_{V_m}(V_m)$ is the cumulative distribution function of the mean wind speed. The parameters of F_{V_m} are calibrated so that $F_{\hat{V}_m}$ matches the Gumbel distribution fitted to the annual maxima reported in Fig. 15 in Castellon et al. (2022). Castellon et al. (2022) adopted a Weibull distribution to model V_m, but its fast convergence to the Gumbel distribution (rate $\sim 1/\log N$ vs. $1/\sqrt{\log N}$ for the lognormal distribution Leadbetter et al., 1983) comes at the cost of a poor representation of frequent events. Indeed, about 50% of the probability lies between 0 and 1 m/s (see Fig. 8), which does not reflect the wind speed population (see Fig. 14(a) in Castellon et al. 2022). In contrast, the lognormal distribution offers a more consistent description of it, even if it slightly overestimates the extremes (e.g., the 100-years return wind speed increases approximately from 43 to 46.1 m/s); for the same reason, it is used also by other authors (e.g., Lystad et al. 2020 for the Hardanger Bridge). The parameters of the ten-minutes mean wind velocity distribution f_{V_m} are summarized in Table 2, and this population distribution is shown in Fig. 8 (top abscissa and left ordinate axes). Fig. 8 also illustrates the fit of the annual maximum mean wind speed data by Gumbel, Weibull^N and lognormal^N models (bottom abscissa and right ordinate axes). Concerning the turbulence intensities, compared to Castellon et al. (2022), the pattern of the mean of I_w beyond $V_m = 22$ m/s is revised: instead of increasing with V_m, I_w is kept constant at 5.6% to better reflect the trends of data, as shown in Fig. 17 of Castellon et al. (2022). The same adjustment is applied to the mean distribution of I_u, which is held constant at 8.8% beyond 22 m/s. The mean and standard deviation of the turbulence intensities as functions of the mean wind velocity are shown in Fig. 9. This baseline wind scenario will hereafter be referred to as A.

To explore the influence of turbulence and wind climate on average parametric effect contributions to bridge response extremes, two additional wind scenarios are considered. In scenario B, the mean turbulence intensities are increased by 50% (then, the mean values associated with the 100-years mean wind speed become $I_u = 13.3\%$ $I_w = 8.3\%$, similar to the values observed for the Hardanger Bridge site; Fenerci and Øiseth 2018, Barni et al. 2022) while maintaining the same coefficients of variation as in the baseline scenario. The probability distribution of mean wind speed is kept unchanged. Scenario C builds upon scenario B, sharing the same characteristics of turbulence, but a more severe wind climate is assumed. Indeed, the parameters of the baseline lognormal distribution are modified to yield $V_m = 52.1$ m/s at the bridge deck height for a 100-years return period. This value is obtained by converting a basic wind speed of 33 m/s, associated with a 50-year return period at 10 m height for terrain category II (representing a possible strong wind condition in Europe), to a terrain category I at the deck height for a return period of 100 years, as specified in Eurocode 1 (ENV1991-1-4, 2010). Scenario C is completed by increasing the mean of wind velocity population by the same factor as for the 100-years return period mean wind velocity (52.1/46.1 = 1.13). Table 2 lists the parameters of the lognormal distribution adopted for the mean wind velocity in the three wind scenarios. Table 2 also reports the reference environmental parameters used in the following for classical short-term response calculations. Fig. 10 shows the environmental contours in the ($V_m\, I_w$) plane, derived from the joint probability distribution $f_{I_w|V_m}(I_w|V_m)\, f_{V_m}(V_m)$ based on an inverse first-order reliability approach. Each contour line corresponds to a set of ($V_m\, I_w$) combinations corresponding to the same reliability index associated with a given annual exceedance probability (Winterstein et al., 1993; Lystad et al., 2020). The three figures refer to the three wind scenarios defined above. As expected, for wind scenario B the contours shift upward, due to the increased mean turbulence intensity. The contours also stretch with respect to the ordinate, since the coefficient

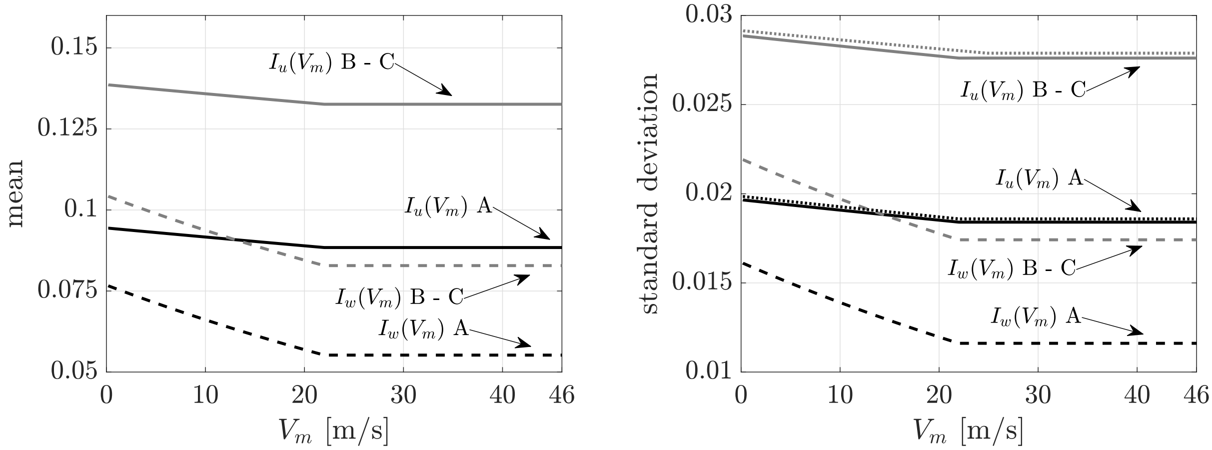

(a) (b)

Fig. 9. Variation in the mean and standard deviation of turbulence intensities as functions of V_m, for all wind scenarios considered (A, B and C). The dotted lines in the standard deviation plots indicate the values adopted for the longitudinal turbulence intensity in the case with two random variables (see Table 1).

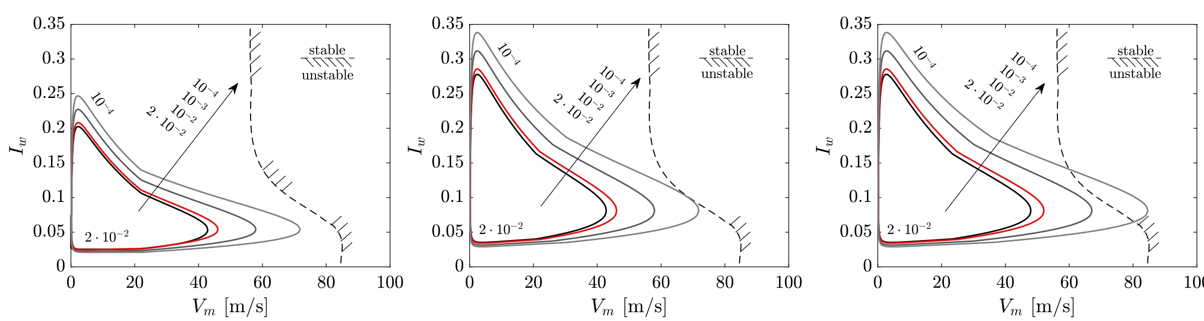

(a) Wind scenario A (baseline). (b) Wind scenario B. (c) Wind scenario C.

Fig. 10. Environmental contour plots in the plane (V_m I_w), corresponding to different annual exceedance probabilities (from 10^{-4} to $2 \cdot 10^{-2}$) for the three wind scenarios. The flutter stability boundary, calculated using the average aerodynamic derivatives (Eq. (14)) for various I_w values, is depicted with a black dashed line.

of variation is the same as in scenario A. Conversely, for wind scenario C the contours also extend toward higher velocities.

Fig. 10 also reports the flutter stability domain for the Halsafjorden Bridge, which accounts for the average parametric effect, as explained in Section 3. Indeed, the critical wind speed varies with the vertical turbulence intensity I_w. The annual probability of falling in the flutter domain $\mathbf{W}_f$ (i.e., the probability of instability) can be computed by integrating the joint distribution $f_{I_w,\hat{V}_m}$ over the unstable region (note that this joint probability refers to $\hat{V}_m$, that is the annual maximum of the mean wind velocity). For the three considered wind scenarios, the estimated flutter probabilities are: $[0.21\ 0.95\ 3.57] \cdot 10^{-4}$ accounting for the average parametric effect and $[1.37\ 1.37\ 5.5] \cdot 10^{-5}$ neglecting it. It is important to note that, since out-of-range aerodynamic derivatives are frozen at their boundary values (see Section 4.2), the flutter boundary flattens for $I_w \gtrsim 15\%$. If the torsional-damping term A_2^* were to continue increasing for $|\alpha| > 8°$, the critical wind speed would further decrease with I_w. This modeling approximation may slightly affect the results in wind climates where high-turbulence conditions are more likely.

As anticipated, the remaining turbulent wind parameters are assumed to be deterministic and are used in the definition of the turbulent fluctuations. The one-sided power spectral densities $S_{u,w}(f)$ of the longitudinal (u) and vertical (w) wind components are defined through the Kaimal spectrum:

$$\frac{f\, S_{u,w}}{(V_m\, I_{u,w})^2} = \frac{A_{u,w} f_z}{\left(1 + 1.5\, A_{u,w} f_z\right)^{5/3}}, \quad f_z = \frac{f\, z}{V_m} \tag{21}$$

where $A_{u,w}$ are the corresponding spectral constants ($A_u = 11.24$, $A_w = 5.12$), f the frequency (in Hz), f_z the reduced frequency, and z is the reference height at the bridge deck. The spanwise correlation of velocity fluctuations is modeled using the Davenport exponential coherence function (Davenport, 1962):

$$C_{u,w}(f, \Delta x) = \exp\left[-K_{u,w} \frac{\Delta x\, f}{V_m}\right], \tag{22}$$

where Δx is the along-span separation, and $K_{u,w}$ are the decay coefficients ($K_u = 8.54$, $K_w = 9.19$). Both the spectral parameters and the coherence decay coefficients correspond to their average values at the wind speed associated with a 100-years return period (Castellon et al., 2022). Finally, it is also worth mentioning that the variability in turbulence parameters becomes especially relevant when directional effects are not explicitly accounted for, as in the present work.

5. Preliminary analyses

This section presents some preliminary analyses mainly aimed at examining some of the assumptions underlying the long-term extreme response framework proposed in this study. Specifically, it focuses on: (i) the role of average parametric effect of turbulence; (ii) the validity of the independent crossing assumption, which enables the description of conditioned response maxima (Eq. (1)) via a Poisson probability distribution; (iii) the influence of different definitions of threshold-crossing rates in the presence of a static response (B- versus D-type crossings, Eq. (3)). Finally, the adopted long-term formulation (Eq. (7))

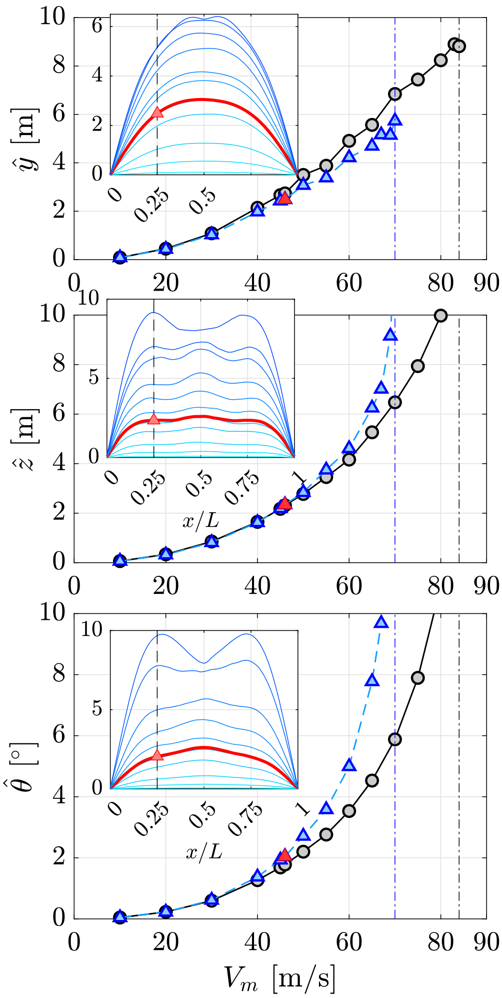

Fig. 11. Quarter-span bridge dynamic response maxima for the lateral, vertical and torsional components according to the classical approach for self-excited forces (no parametric effects, black line with circles) and the model including average parametric effect (blue dashed line with triangles). The full-span response is also shown for the latter case in the top-left corner insets. The 100-years return period response is highlighted in red. Dash–dot vertical lines denote the flutter critical velocities.

is validated with Monte Carlo simulations. These analyses clarify the applicability limits of the proposed approach and help determine the conditions under which simplified modeling strategies are justified or more advanced approaches are necessary. In this section and in Section 6, the results refer to the deck displacements of the Halsafjorden Bridge, as they can be considered representative quantities for highlighting in a simple and compact way the wind-induced effects discussed in this work.

5.1. Parametric effects of turbulence on bridge response

As discussed in Section 3, turbulence-induced fluctuations in the angle of attack modify the aerodynamic damping and stiffness in a nonlinear fashion. The predominant contribution of it can be captured by averaging the aerodynamic derivatives over the angle of attack probability distribution (average parametric effect, see Barni and Mannini 2024).

To quantify its impact on both buffeting response and flutter stability, two analyses are performed: one using conventional aerodynamic derivatives evaluated at the mean angle of attack (i.e., α_m), and the other using the average aerodynamic derivatives computed via Eq. (14). The comparison is illustrated in Fig. 11 for the wind scenario B, with high turbulence intensity. The figure shows the peak response at quarter-span in terms of lateral, vertical, and torsional displacements as functions of mean wind velocity, calculated using the classical short-term approach (Section 2.1). The inclusion of the average parametric effect results in a marked increase in the torsional response. This can be attributed to the reduction in the aerodynamic damping associated with the aerodynamic derivative A_2^*, as shown in Fig. 7. This effect becomes particularly pronounced near the flutter critical condition, occurring at approximately 69 m/s with a two-antinode antisymmetric mode shape. Moreover, in the high wind speed range (in particular, above the 100-years mean wind velocity), the vertical response exhibits some evidence of modal coupling with the torsional mode, with an increased contribution from the two-antinode antisymmetric torsional mode, leading to larger response amplitudes and a shift in the zero upcrossing frequency $\nu^+_{\hat{R}_0}$ towards the natural frequency of the torsional mode. Conversely, the lateral response slightly decreases, due to the increase in the absolute value of the average aerodynamic derivative P_1^* (as will be shown more clearly in Section 6), which enhances aerodynamic damping in the lateral modes.

The average parametric effect is expected to influence the long-term response by altering the conditional probability of exceedance $F_{\hat{R}(T)}(r|\mathbf{w})$. This becomes more pronounced when the product $(1 - F_{\hat{R}(T)}(r|\mathbf{w}))f_{\mathbf{W}}(\mathbf{w})$, which defines the contribution of each environmental state to the long-term integral, accumulates in regions of high vertical turbulence intensity and wind velocity (especially when relatively close to the flutter stability boundary). Therefore, it will be more marked for wind scenarios B and C than for wind scenario A.

5.2. Choice of short-term crossing model

This section investigates the influence of the model chosen for defining the response conditional probability $F_{\hat{R}(T)}(r|\mathbf{w})$ in Eq. (7) on the long-term extreme response. Since no appreciable differences arise from including or neglecting the average parametric effect in this specific analysis, the results are presented only for the case in which this effect is considered. Finally, the baseline wind scenario A is adopted in this section, but scenarios B and C are referred to in the discussion when relevant.

First, assuming a Poisson model for $F_{\hat{R}(T)}(r|\mathbf{w})$, Fig. 12 compares the effects on the long-term extreme response of the two different formulations of the crossing frequency of the threshold r, namely either B-type or D-type (see Eqs. (2)–(3)). It is apparent that the two approaches practically yield identical responses when the static response is included. This occurs because the presence of a non-zero mean response μ_R shifts the process away from one of the two barriers $\pm r$ and strongly reduces the rate of either positive or negative crossings. Therefore, even in the case D-crossing is of interest for structural applications, the presence of a significant mean response compared to the standard deviation makes D- and B-crossing models practically equivalent. If the static component is small (i.e., small static coefficients near α_m), some discrepancies may occur. Indeed, as shown in Fig. 12, when $\mu_R = 0$ the long-term response based on the D-crossing rate $\nu^+_{|R|}$ is consistently about 6%–7% higher for the vertical and torsional components and slightly less for the lateral component. This difference increases to 10% under wind scenario B, due to the higher turbulence enhancing the dynamic response. In structural safety checks, it might be necessary to refer to both B- and D-crossing depending on the case. However, a D-crossing approach is a conservative choice and the possible overestimation is generally limited and acceptable from a safety perspective.

Furthermore, to assess the validity of Poisson model for the probability of response maxima (Eq. (1)), Fig. 13 shows the ratio of the peak factor proposed by Vanmarcke and accounting for possible crossing clusters (e.g., see Chen 2014) to that obtained from Rice-Davenport theory (Davenport, 1961), evaluated across the domain of environmental parameters. This ratio quantifies the expected deviation from the

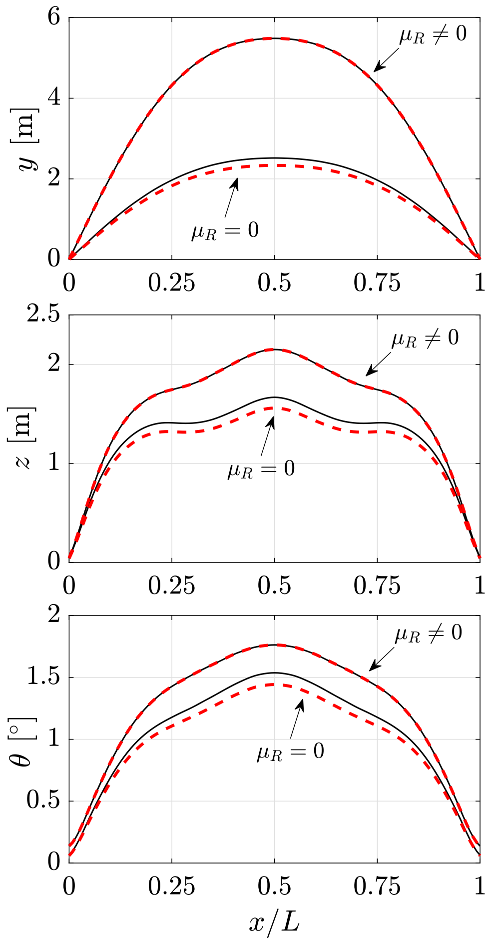

Fig. 12. 100-years return period long-term lateral, vertical, and torsional bridge response for wind scenario A. Results are shown for D-type ($\nu^+_{|R|}$, black lines) and B-type (ν^+_R, red lines) crossing definitions, evaluated with (dashed lines) and without (solid lines) the mean response (μ_R).

assumption of independent upcrossings in terms of extreme response. The results confirm that, for the present case study, this assumption is generally satisfied, as the ratio remains close to one over most of the environmental parameter space. In some rare instances, particularly for the lateral response, where the bandwidth parameter $q = \sqrt{1 - m^2_{R_1}/(m_{R_0} \cdot m_{R_2})}$ (Vanmarcke, 1975) drops to values as low as 0.4–0.5, the Poisson approximation is less accurate but in any case on the safe side, leading to a response overestimation of no more than 5%. Deviations close to 10% occur only for very unlikely combinations of V_m and I_w near the upper edge of the torsional flutter boundary. Since these cases correspond to very rare events, their contribution to the long-term response is negligible, once weighted by the probability of occurrence $f_{\mathbf{W}}(\mathbf{w})$. For further discussion on this point, see Appendix B.

5.3. Long-term extremes validation via Monte Carlo

To validate the proposed long-term response formulation, a Monte Carlo simulation is performed. A total of 20000 years of annual maxima are simulated for both the mean wind velocity and the structural response, assuming all the other environmental variables to be deterministic and consistent with wind scenario A. For each year, $N = 365.25 \times 24 \times 6 = 52596$ realizations of the mean wind velocity are drawn. For each realization, a peak response is sampled from the short-term conditional probability distribution of maximum response derived from Eq. (1), where the spectral moments defining the Poisson distribution are computed based on the given V_m. The corresponding static response is then added to the sampled peak dynamic response. The (annual) maximum is stored for each response component (lateral, vertical, torsional).

Fig. 14 compares the calculated long-term response distributions with those obtained from the Monte Carlo simulations. The agreement is excellent over the entire range, and the small discrepancies in the tails are simply due to the fact that the sample, although large, is still limited. This confirms that the proposed framework accurately captures the long-term response, including the effect of nonzero mean components.

6. Results

6.1. Comparison with the classical short-term approach

Fig. 15 illustrates the cumulative probability distribution of long-term bridge response at mid-span in terms of lateral, vertical, and torsional components under the baseline wind scenario A, considering only the mean wind velocity V_m as a random variable. Both the purely dynamic response (ignoring the static response, Fig. 15(a)) and the total response (including the static component, Fig. 15(b)) are reported. In fact, although static and dynamic contributions cannot rigorously be separated in a long-term analysis, the first set of results is instrumental to emphasize the differences compared to classical approaches in case the static response was negligible. The figure also shows the short-term PDF of response maxima, computed via Eq. (1) for the 100-years return period mean wind velocity, along with the response predicted by the classical Davenport approach ($R_{ST} = \mathbb{E}[\hat{R}(T)]$, where T is an observation time of ten minutes). The long-term response associated with a non-exceedance probability of 0.99 (return period of 100 years) is projected onto the short-term distributions of maxima for comparison in terms of response fractiles. The long-term response is slightly higher than the classical Davenport prediction, both for total and purely dynamic response. The response calculated with the classical short-term approach always corresponds to the 53.6th percentile of the distribution, whereas the long-term estimate is associated with the 65.2th percentile in the lateral direction and 62nd–61st in the vertical and torsional directions. However, explicitly including the static response in the long-term integral reduces these differences, particularly for the lateral response. This is due to the fact that the contribution of the static response to long-term extremes is fairly close to the simple static response associated with the considered return period, as will be extensively discussed in Section 6.3.

Disregarding the static response (Fig. 15(a)), the differences introduced in the long-term response by the average parametric effect are modest for wind scenario A, yet not negligible. Its inclusion results in a reduction of approximately 4.3% in the lateral response and an increase of about 8.1% in the torsional response. The former is primarily due to an increase in aerodynamic damping in the lateral response, associated with the aerodynamic coefficient P_1^*, while the latter is caused by a reduction in the torsional aerodynamic damping related to A_2^*, as explained in Section 3 and showed in Fig. 7. These variations are significantly larger than those observed in the total response (in Fig. 15(b), −1.8% and +6.3%, respectively), as the static component partially masks such an effect. Notably, these variations are consistent for both classical Davenport and long-term approaches, since the average parametric effect does not change between the two analyses when the vertical turbulence intensity is treated as deterministic.

As expected, the more severe wind scenarios B and C lead to a general increase in structural response across all components, as shown in Table 3, which reports the 100-years return period dynamic response at mid-span. In addition, the impact of the average parametric effect becomes significantly more pronounced as turbulence intensity and wind climate severity increase. In scenario B, its inclusion leads to a reduction of about 10.2% in the lateral response and an increase

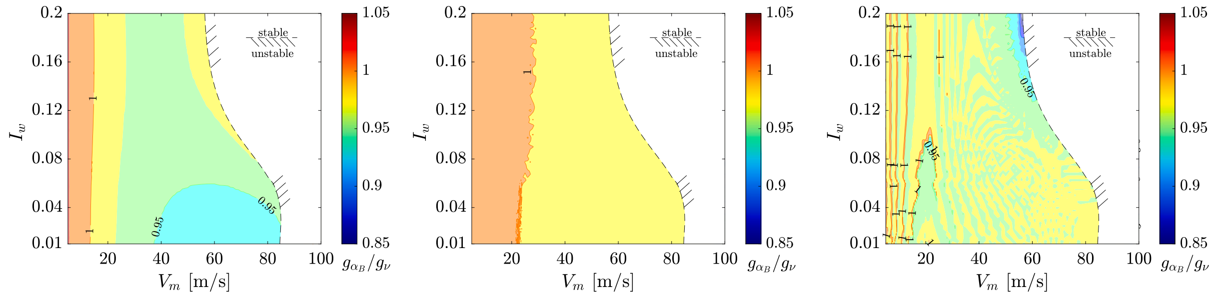

(a) Longitudinal (b) Vertical (c) Torsional

Fig. 13. Ratio of Vanmarcke to Rice–Davenport peak factors evaluated at the quarter-span under the baseline wind scenario A.

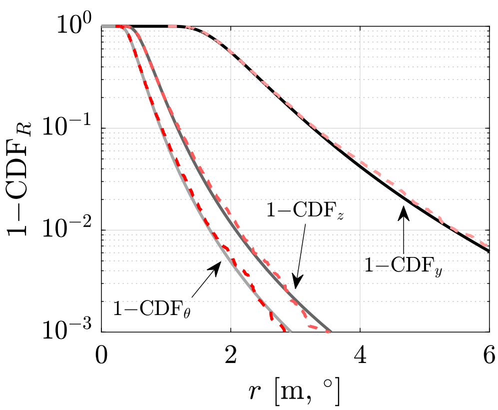

Fig. 14. Comparison between long-term probability of exceedance of the structural response obtained from the proposed long-term formulation and Monte Carlo simulations. The grayscale curves represent the computed exceedance probabilities for lateral, vertical, and torsional response components as functions of the generic threshold r, while the red dashed lines indicate the corresponding results from Monte Carlo simulations.

of 16.1% in the torsional response. Again, this behavior reflects the fact that parametric effects become more pronounced under wind conditions with higher turbulence intensity, as also illustrated in Fig. 7, which show greater variation in both stabilizing and destabilizing contributions to the lateral and torsional responses, respectively. By contrast, the vertical aerodynamic damping remains almost unchanged. These trends become even more evident in scenario C, where the lateral response decreases by 12.0% and the torsional response increases by 22.7%. This is because higher wind speeds shift the dominant contributions to the long-term integral closer to the instability threshold (Barni et al., 2022; Barni and Mannini, 2024), further emphasizing the role of parametric effects of turbulence in torsion due to coupling with the vertical motion. Once again, the results are comparable regardless of whether the response is estimated using the Davenport approach or the long-term formulation.

6.2. Effects of randomness in turbulence characteristics

Although the mean wind speed is typically supposed to be the main source of randomness in the environmental parameters, here we explore the impact on long-term response of introducing the randomness in turbulence intensity. Tables 3 and 4 report the 100-years return period dynamic and total responses, respectively, at mid-span for the three considered wind scenarios. By comparing the cases with the mean wind velocity as unique random variable to those including also the vertical turbulence intensity, a systematic increase in the predicted response is observed, especially in the torsional component. Focusing first on the dynamic response only (Table 3) and excluding the average parametric effect, under wind scenario A, modeling I_w as a random variable leads to a moderate increase in the dynamic response, between 7% and 9% across all response components. For scenarios B and C, the increase is of similar magnitude; therefore, for this case study, the introduction of vertical turbulence variability produces a comparable effect regardless of the wind scenario considered. When the static response is also included in the long-term analysis, these differences are generally reduced, particularly in the lateral direction. Tables 3 and 4 also show that the inclusion of I_w as environmental random variable only slightly increases the average parametric effect on the long-term extreme response at the bridge mid-span. A similar conclusion applies to the bridge quarter-span, where the impact of the average parametric effect of turbulence is only slightly more pronounced for T_{RP} = 100 years.

The picture can change in a large amount if higher return periods are considered. Indeed, as highlighted in Fig. 16, for T_{RP} = 1000 years, the influence of the average parametric effect on the long-term response markedly increases, especially in torsion at the bridge quarter-span, exhibiting increments of 15, 41 and 104% for wind scenarios A, B and C, respectively, compared to 12, 33 and 76% in the classical short-term analysis. This is explained by Fig. 17 for wind scenario C, showing how the main contributions to the long-term integral shift closer to the flutter boundary when the return period of the torsional response is increased from 20 to 1000 years, thus emphasizing aeroelastic effects. Additionally, by examining Fig. 18, which reports the normalized average aerodynamic derivative $\bar{A}_2^*$, directly responsible for the aerodynamic damping in torsion, it becomes clear that for T_{RP} = 1000 years the most significant contributions to the long-term integral lie in regions where the average aerodynamic derivative $\bar{A}_2^*$ is significantly lower than for 100 years. It is also worth noting that, for both 100- and 1000-years return periods, such contributions are concentrated in a region slightly above the mean value of the vertical turbulence intensity, indicating that $\bar{A}_2^*$ tends to reduce when the variability in the vertical turbulence intensity is introduced. Finally, it is evident that a non-negligible portion of the long-term integral contributions falls within the unstable domain, suggesting a non-negligible impact of flutter instability on the response. This will be discussed in more detail in the next section.

Finally, it is worth explaining why the parametric variation in the angle of attack due to turbulence affects more the response at the quarter-span than at the mid-span. This nonlinear effect is responsible for the anticipation of the flutter stability threshold (see Fig. 11 and Barni et al. 2022), which shifts the large low-damping pre-critical response toward more probable wind states **w**. Since the flutter mode exhibits a two-antinode antisymmetric shape (see Fig. 11), when the major contributions to the long-term integral come from a region close to the flutter boundary, the antisymmetric torsional mode (mode 13, see Fig. 5) is very low damped and heavily contributes to the response at $\ell/4$ but not at $\ell/2$ (Fig. 16(c)). Although a return period of 1000 years may seem overly long for the dynamic response to

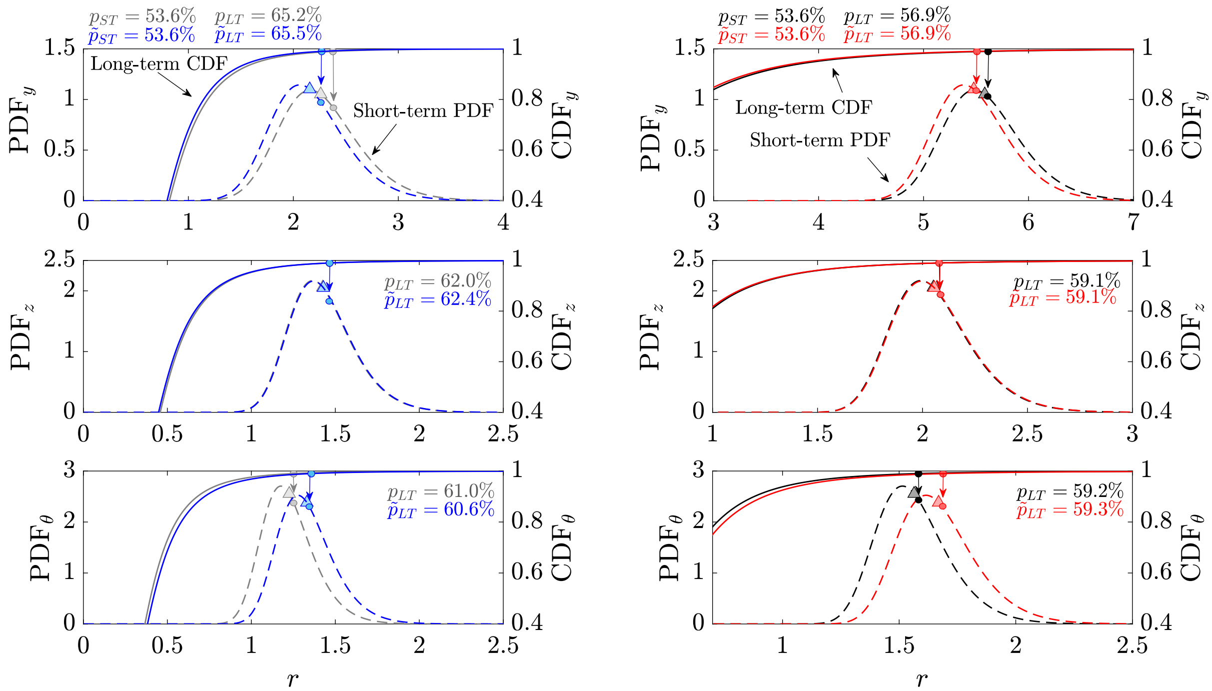

(a) $\mu_R = 0$ (b) $\mu_R \neq 0$

Fig. 15. CDF of mid-span long-term bridge responses (lateral, vertical and torsional), without (a) and with (b) the static response, considering only the mean wind velocity V_m as environmental random variable. Dashed lines represent the short-term PDF of response maxima corresponding to the 100-years mean wind velocity. Triangular markers on the PDFs indicate the response estimated using the Davenport approach, i.e., the mean of the distribution, while circles denote the long-term responses associated with a 100-years return period (probability of non-exceedance of 0.99 in the CDFs). Blue and red lines refer to results including the average parametric effect, while gray and black lines correspond to results without them. p_{ST} and p_{LT} denote the fractiles in the short-term distribution corresponding to the classical short-term and long-term responses, respectively. The tilde indicates the fractiles in the cases where the average parametric effect of turbulence is considered.

Table 3
100-years return period mid-span extreme bridge dynamic response (neglecting the static response) under various wind scenarios. Percentage differences refer to the corresponding short-term case (R_{ST}). "APE" and "NO APE" indicate results obtained with and without the Average Parametric Effect.

Wind scenario	Resp. comp.	R_{ST}		$R_{LT} : V_m$		$R_{LT} : V_m, I_w$		$R_{LT} : V_m, I_u, I_w$	
		NO APE	APE	NO APE	APE	NO APE	APE	NO APE	APE
A	y [m]	2.30	2.20	2.38 (+3.48%)	2.27 (+3.18%)	2.57 (+11.74%)	2.42 (+10.00%)	–	2.40 (+9.09%)
	z [m]	1.44	1.45	1.46 (+1.39%)	1.47 (+1.38%)	1.57 (+9.03%)	1.56 (+7.59%)	–	1.56 (+7.59%)
	θ [°]	1.24	1.34	1.25 (+0.81%)	1.36 (+1.49%)	1.33 (+7.26%)	1.45 (+8.21%)	–	1.45 (+8.21%)
B	y [m]	3.45	3.10	3.57 (+3.48%)	3.22 (+3.87%)	3.86 (+11.88%)	3.43 (+10.65%)	–	3.42 (+10.32%)
	z [m]	2.16	2.16	2.20 (+1.85%)	2.19 (+1.39%)	2.35 (+8.80%)	2.33 (+7.87%)	–	2.32 (+7.41%)
	θ [°]	1.86	2.16	1.88 (+1.08%)	2.17 (+0.46%)	2.00 (+7.53%)	2.33 (+7.87%)	–	2.33 (+7.87%)
C	y [m]	4.35	3.83	4.50 (+3.45%)	3.99 (+4.17%)	4.89 (+12.41%)	4.26 (+11.23%)	–	4.25 (+10.96%)
	z [m]	2.88	2.93	2.92 (+1.39%)	2.96 (+1.02%)	3.13 (+8.68%)	3.16 (+7.85%)	–	3.14 (+7.17%)
	θ [°]	2.51	3.08	2.53 (+0.80%)	3.08 (0.00%)	2.70 (+7.57%)	3.37 (+9.42%)	–	3.36 (+9.09%)

turbulent wind (i.e., design stress calculation), some standards adopt unity safety factors but refer to high return periods (for instance, 700 years for ASCE-7-22, 2022), whereas Eurocode 1 (ENV1991-1-4, 2010) typically considers a return period of 50 years (even 100 years for strategic structures) and a safety factor of 1.5.

The calculations with three environmental random variables ($\mathbf{w} = [V_m\ I_u\ I_w]^t$), carried out here only accounting for parametric effects of turbulence, provide results that are nearly identical to those with two random variables. Although the variability in the longitudinal turbulence intensity I_u is known to influence the structural response and has been emphasized in previous studies (e.g., Lystad et al. 2021, Castellon et al. 2023), a rigorous analysis with three environmental random variables is not expected to give here results very different from those obtained with only V_m and I_w for two reasons. First, the coefficient of variation of I_u is close to that of I_w; as shown in Fig. 9, the standard deviation of I_u in the three-variable model is only slightly higher than

Table 4
100-years return period mid-span extreme bridge dynamic response (including the static response) under various wind scenarios. Percentage differences refer to the corresponding short-term case (R_{ST}). "APE" and "NO APE" indicate results obtained with and without the Average Parametric Effect.

Wind scenario	Resp. comp.	R_{ST}		R_{LT} : V_m		R_{LT} : V_m, I_w		R_{LT} : V_m, I_u, I_w	
		NO APE	APE	NO APE	APE	NO APE	APE	NO APE	APE
A	y [m]	5.62	5.52	5.62 (0.00%)	5.51 (−0.18%)	5.71 (+1.60%)	5.57 (+0.90%)	–	5.57 (+0.90%)
	z [m]	2.07	2.08	2.08 (+0.48%)	2.08 (0.00%)	2.15 (+3.86%)	2.15 (+3.37%)	–	2.15 (+3.37%)
	θ [°]	1.58	1.68	1.58 (0.00%)	1.69 (+0.60%)	1.65 (+4.43%)	1.77 (+5.36%)	–	1.77 (+5.36%)
B	y [m]	6.77	6.42	6.79 (+0.30%)	6.44 (+0.31%)	6.95 (+2.66%)	6.54 (+1.87%)	–	6.54 (+1.87%)
	z [m]	2.79	2.79	2.81 (+0.72%)	2.80 (+0.36%)	2.94 (+5.38%)	2.92 (+4.66%)	–	2.91 (+4.30%)
	θ [°]	2.20	2.50	2.21 (+0.45%)	2.50 (0.00%)	2.32 (+5.45%)	2.66 (+6.40%)	–	2.66 (+6.40%)
C	y [m]	8.59	8.07	8.60 (+0.12%)	8.09 (+0.25%)	8.83 (+2.79%)	8.22 (+1.86%)	–	8.23 (+1.98%)
	z [m]	3.68	3.73	3.70 (+0.54%)	3.75 (+0.54%)	3.87 (+5.16%)	3.90 (+4.56%)	–	3.90 (+4.56%)
	θ [°]	2.94	3.51	2.96 (+0.68%)	3.51 (0.00%)	3.12 (+6.12%)	3.78 (+7.69%)	–	3.79 (+7.98%)

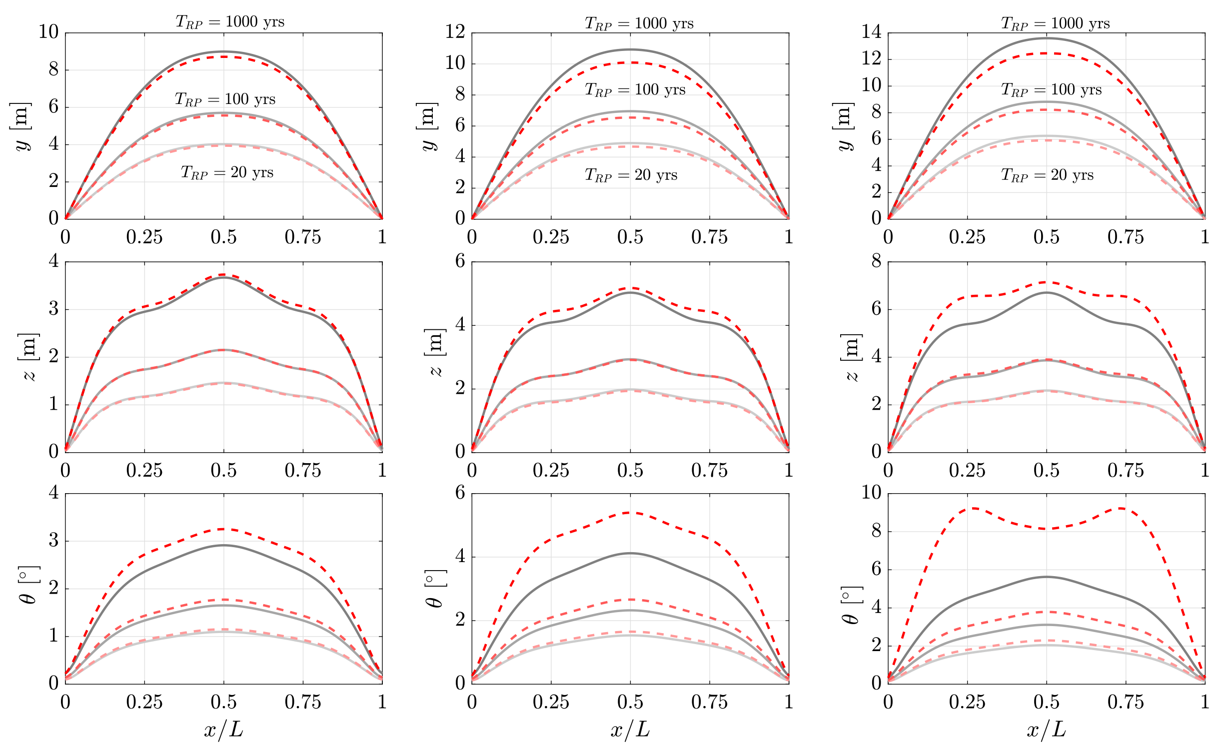

(a) Wind scenario A (b) Wind scenario B (c) Wind scenario C

Fig. 16. Extreme total response of the Halsafjorden Bridge with (solid lines in shades of red) and without (solid lines in shades of gray) the average parametric effect, for different return periods.

that implicitly assumed in the two random variable analysis. Similarly, the experimentally estimated correlation coefficient between I_u and I_w is fairly high (about 0.67, see Castellon et al. 2022). Obviously, the similarity between supposed and actual behavior of the random variable I_u is not by chance, but rather due to the physical relation existing between longitudinal and vertical turbulence. Secondly, the average parametric effect is independent of I_u (see Eqs. (14)–(15)), so that including I_u as a third environmental random variable does not affect the long-term response through this mechanism. Moreover, the contribution of longitudinal turbulence to vertical and torsional response is overall very small given the linearized force coefficients appearing in the buffeting forces (see Eq. (16)).

Finally, Table 5 reports the wall-clock time required by the long-term analysis as the number of environmental variables **w** increases. For comparison, the table also lists the computational cost of performing nonlinear short-term calculations in the time domain, where parametric effects of turbulence are fully represented (both the average parametric effect and the parametric resonances, see Barni and Mannini 2024). The time-domain figures are estimated for a 2D RFA model with four additional aeroelastic states (Barni et al., 2021); the actual cost

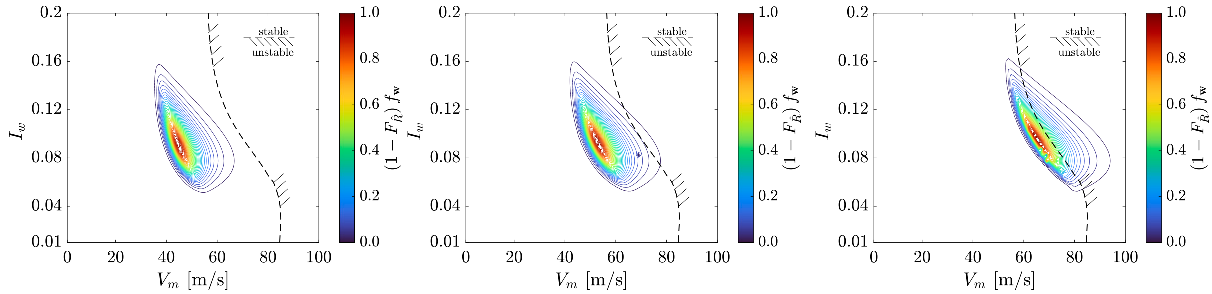

(a) $T_{RP} = 20$ years (b) $T_{RP} = 100$ years (c) $T_{RP} = 1000$ years

Fig. 17. Contribution to the torsional-response long-term integral (i.e., the integrand of Eq. (7)) over the environmental parameter space (V_m, I_w), normalized with respect to its maximum value and evaluated at quarter-span for wind scenario C and various return periods.

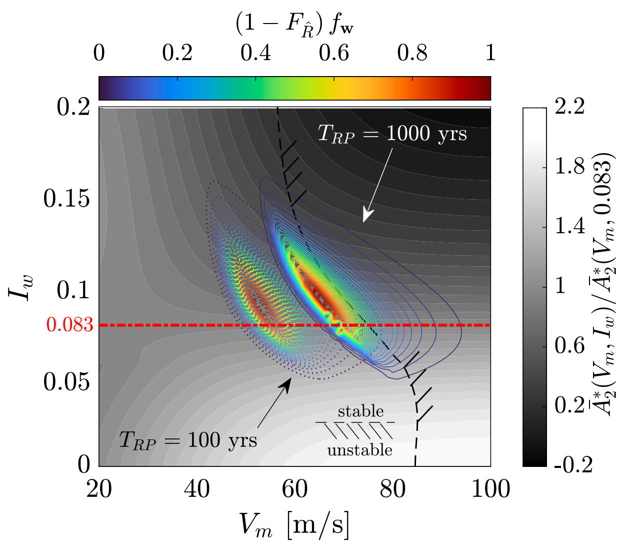

Fig. 18. Direct contribution to the average aerodynamic damping in torsion as a function of mean wind velocity and vertical turbulence intensity (the average aerodynamic derivative $\bar{A}_2^*$ is normalized with the value assumed for the mean vertical turbulence intensity, highlighted by the red dashed line). Superimposed is also the map of the contributions to the long-term integral (i.e., the integrand of Eq. (7), normalized with the maximum value) for the quarter-span torsional response associated with return periods of 100 and 1000 years for the wind scenario C.

would scale with the number of states required to accurately fit the aerodynamic derivatives over the (V_r, α) plane. Under these conditions, the time required for a single short-term response calculation is about 30 s in the frequency domain and about 36000 s (10 h) in the time domain.

6.3. Static response and flutter effects on long-term extremes

Since static and dynamic response components cannot formally be separated in the long-term integral, the contribution of the former is quantified as the difference between the total long-term response and that obtained by nullifying the static mean component appearing in Eq. (7) through the upcrossing rate. Results all along the bridge span for various return periods are reported in Fig. 19 and compared to the static response evaluated at the mean wind speed corresponding to the same return period. Only the case with average parametric effect is considered here. The contribution of the static response to the long-term response is systematically slightly lower than the corresponding deterministic static response. The relative difference reaches a maximum of approximately 10% for the lateral component, 7% for the vertical component, and 6% for the torsional component. In two specific cases, namely the torsional response under wind scenarios B and C, the difference is practically negligible.

Table 5
Computational cost of long-term analyses accounting for turbulence-induced parametric effects, using linear short-term calculations in the frequency domain versus the cost of using nonlinear short-term calculations in the time domain (tests run on a 12-core/24-thread 3.7 GHz CPU, 64 GB RAM). $N_{\mathbf{w}}$ indicates the number of short-term calculations required for an accurate estimation of the long-term integral.

Long-term analyses	Frequency domain		Time domain (nonlinear)	
	$N_{\mathbf{w}}$	Time [days]	$N_{\mathbf{w}}$	Time [days]
$\mathbf{w} = V_m$	66	0.02	66	27.5
$\mathbf{w} = [V_m\ I_w]^t$	2245	0.78	2245	935
$\mathbf{w} = [V_m\ I_u\ I_w]^t$	55 552	19.3	55 552	23 146

The way the variation in the mean upcrossing rate ν_R^+ due to the presence of the static response (see Eq. (2)) can modify the shape of the integrand in Eq. (7) is illustrated in Fig. 20. Significant contributions to the integral start at lower wind velocities, while those at high velocities remain largely unchanged, resulting in a more concentrated distribution (dotted red curve) around the mean wind speed corresponding to the 100-years return period (46.1 m/s for the wind scenario A considered in the figure). When the vertical turbulence intensity is also treated as a random variable, the distribution of the contributions to the integral changes accordingly along this additional dimension.

Referring back to Fig. 16 and comparing it with Fig. 19, it is evident that the gust factor for the lateral response ranges approximately between 1.7 and slightly more than 2. In contrast, the gust factor is much higher for the vertical (up to 5.9) and above all for the torsional response (up to 10.5), highlighting that, as expected, this response components are dominated by the dynamic contribution. However, these high gust factors are also due to the influence of the average parametric effect, which anticipates the flutter instability and promotes a low-damping precritical response in the high wind speed range. In spite of this, since the Halsafjorden Bridge is quite stable with respect to flutter, the annual probability of flutter across all wind scenarios remains fairly low, with a maximum value of 3.57×10^{-4} in wind scenario C when the average parametric effect is included. While this probability is nearly negligible for a return period of 100 years, for 1000 years, a substantial portion of the response exceedance probability originates from the unstable region (right-hand side of the flutter boundary in the environmental parameter space; see Figs. 17 and 18). In particular, in wind scenario C this contribution accounts for about 36% of the total probability when the average parametric effect is included, whereas it drops to about 5% when the parametric effect is neglected (the flutter annual probability is 5.51×10^{-5}). It is worth reminding that

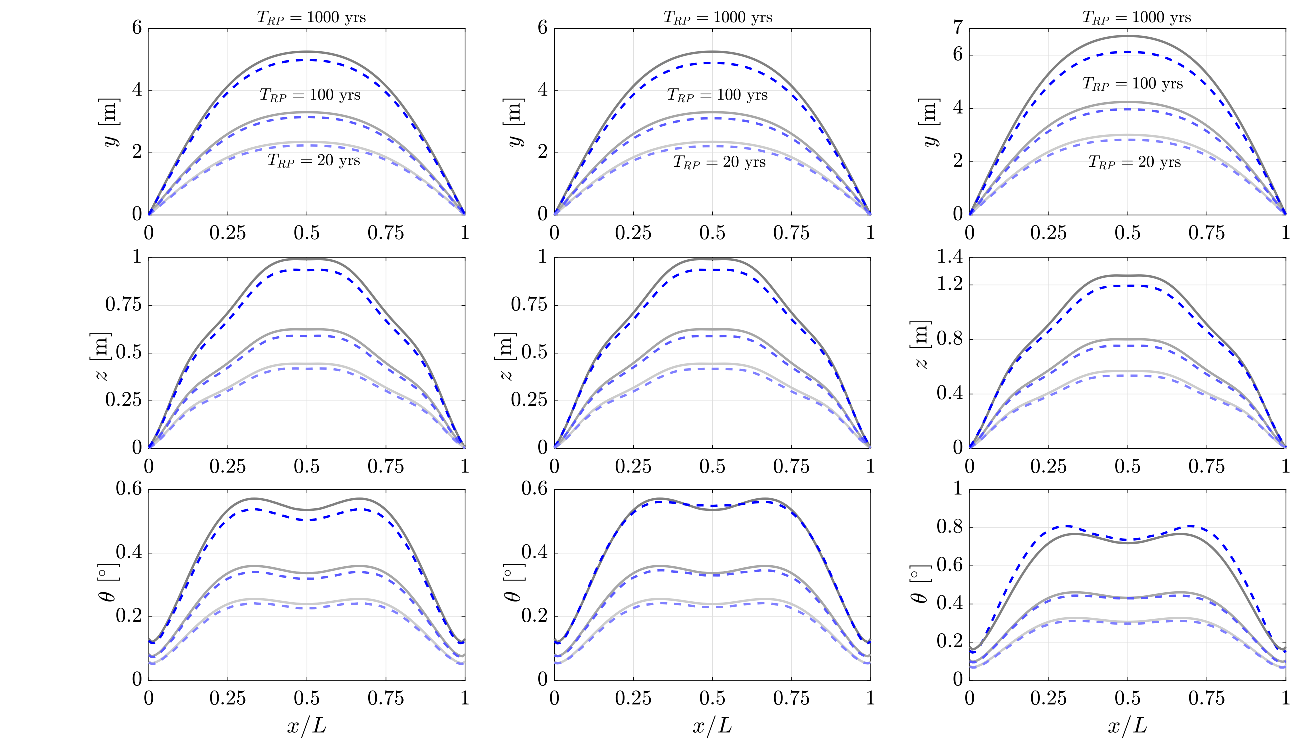

(a) Wind scenario A (b) Wind scenario B (c) Wind scenario C

Fig. 19. Comparison between the static response of the Halsafjorden Bridge obtained by subtracting the long-term dynamic response (computed by excluding the static component) from the total long-term response (Eq. (7)) (shown as blue dashed lines), and the static response evaluated at the wind velocity corresponding to the same return period (shown as gray solid lines), for different return periods.

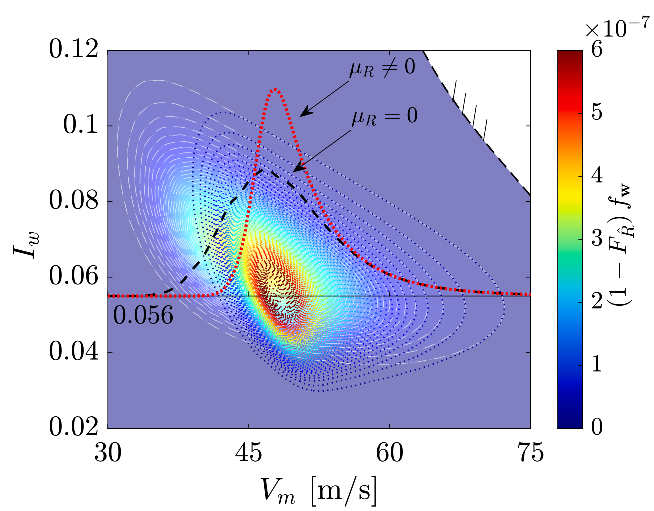

Fig. 20. Contributions to the long-term integral in the space of environmental random variables V_m and I_w (i.e., the integrand of Eq. (7)) associated with the mid-span 100-years return period lateral response in wind scenario A considering the average parametric effect. The background colormap refers to the case assuming null static response, while the overlaid dotted contour plot corresponds to the case in which the static response is included. The case where only V_m is considered as a random variable is shown as a map section at the deterministic value $I_w = 0.056$ (see Table 2).

here the conditional non-exceedance probability $F_{\hat{R}(T)}(r|\mathbf{w})$ has been conservatively set to zero within the unstable domain. Although this is a cautious assumption as discussed in Section 2.4, an inspection of the long-term integral contributions in the vicinity of the flutter boundary suggests that it is also realistic for the thresholds of interest: indeed, no evident discontinuities are observed across the boundary (see Figs. 17 and 18), indicating that the ten-minutes average number of upcrossings $\nu_R(r_{T\,R=1000\text{yrs}}|\mathbf{w})T$ immediately before the boundary is already large enough for the non-exceedance probability to be nearly zero.

7. Conclusions

This study incorporates the average parametric effect, arising from turbulence-induced variations in the angle of attack, into a long-term response framework, avoiding cumbersome time-domain simulations, thus not affecting the computational cost of the overall analysis. Static response and flutter instability are directly embedded in the formulation, and the key assumptions underlying the short-term probabilistic model (e.g., independent crossings) are critically assessed and validated. The long-term response predictions are successfully verified through Monte Carlo simulations. The following main conclusions can be drawn from the study:

- The average parametric effect of turbulence may significantly influence the long-term bridge response, especially for high return periods, for which large wind speeds and turbulence intensities are more likely. Indeed, in this case the aerodynamic damping plays a significant role in the bridge dynamics and can become sensitive to the fluctuations in the angle of attack induced by turbulence. For the Halsafjorden Bridge, the average parametric effect amplifies the torsional response and slightly reduces the lateral response.
- For the Halsafjorden Bridge, if the mean wind speed is considered as the sole environmental random variable, the difference between the long-term response and that obtained using the classical Davenport short-term approach is only minor. In contrast, the difference noticeably increases when the vertical turbulence intensity is treated as a random variable.

- Given the physical constraints affecting turbulence parameters, expensive long-term calculations with three environmental random variables may be avoided. Indeed, analyses in which the longitudinal turbulence intensity is deterministically connected to the vertical turbulence intensity can imply in many cases just a small loss of accuracy.
- Considering the vertical turbulence intensity as a random variable, the average parametric effect of turbulence is practically identical in the long-term and classical short-term approach for low-to-medium return periods (e.g., up to 100 years). In contrast, this nonlinear effect of turbulence has a stronger impact on the long-term response for high return periods (e.g., 1000 years).
- Although the flutter annual probability remains low in the present case, the rare wind states leading to aeroelastic instability may still contribute substantially to the long-term extreme response associated with high return periods, especially when the average parametric effect is included. Within the proposed long-term formulation, a reduced safety margin with respect to flutter instability would therefore be highlighted by a steep increase in the long-term buffeting response, due also to the contribution arising from the unstable region.
- The rigorous inclusion of static response in long-term analysis results in a contribution generally slightly smaller than the static response computed based on the mean wind speed associated with the considered return period. The underlying mechanism leading to this reduction is complex, but it would be of interest to understand under which conditions this difference can become more pronounced.
- For those analyses for which the sign of the response is not a discriminant, the presence of a non-negligible mean response, even modest like for the Halsafjorden Bridge in torsion, is enough to make insignificant the differences between the results obtained for a monolateral or a bilateral threshold (known as B-crossing and D-crossing, respectively).
- As long as the structural response can adequately be modeled using a single-sided barrier, the clustering of threshold crossings does not significantly distort the probability distribution of response maxima. In such cases, the assumption of independence between upcrossing events remains a valid and practically effective simplification for long-term response estimation.

Future developments may focus on extending the proposed framework to include the full range of turbulence-induced parametric effects, including potential parametric resonances (Barni and Mannini, 2024; Barni et al., 2024), through time-domain simulations. This would require the use of computationally efficient methodologies to overcome the prohibitive cost of long-term time-domain analyses. Moreover, in a broader risk-assessment perspective, it would also be interesting to consider structural uncertainties, such as those related to damping. Finally, though the current long-term approach addresses the inconsistency associated with the observation time T, results are still affected by its choice. This is an issue that needs to be tackled in the future.

CRediT authorship contribution statement

Niccolò Barni: Writing – original draft, Visualization, Validation, Software, Methodology, Investigation, Formal analysis, Data curation, Conceptualization. **Ole Øiseth:** Supervision, Investigation, Funding acquisition. **Øyvind Wiig Petersen:** Software, Investigation. **Claudio Mannini:** Writing – review & editing, Validation, Supervision, Methodology, Funding acquisition, Formal analysis, Conceptualization.

Declaration of competing interest

The authors declare that they have no known competing financial interests or personal relationships that could have appeared to influence the work reported in this paper.

Algorithm 1 Long-term analysis with Average Parametric Effect (APE)

Require: Environmental grid $\mathcal{W} = \{\mathbf{w}^{(k)}\}_{k=1}^{N_\mathbf{w}}$; response threshold grid $\mathcal{R} = \{r^{(j)}\}_{j=1}^{N_r}$; modal data from FE model $\mathcal{M} = \{\tilde{\mathbf{M}}, \tilde{\mathbf{C}}, \tilde{\mathbf{K}}, \boldsymbol{\Phi}\}$; aerodynamic derivatives $AD(V_r, \alpha)$; static coefficients $\mathbf{c}_{ae} = \left[C_D(\alpha),\ C_L(\alpha),\ B\,C_M(\alpha)\right]^t$ (see Section 4.2)

for $k = 1$ **to** $N_\mathbf{w}$ **do**
  set $\mathbf{w} = \mathbf{w}^{(k)}$ (e.g., $\mathbf{w}^{(k)} = \{V_m^{(k)},\ I_u^{(k)},\ I_w^{(k)}\}$)
  Static response: solve $\bar{\mathbf{K}}\bar{\mathbf{u}}_{st} = \bar{\mathbf{f}}_{ae}$; then set $\mu_R(\mathbf{w}^{(k)}) = \boldsymbol{\Phi}\bar{\mathbf{u}}_{st}$
   ▷ where $\bar{\mathbf{f}}_{ae} = \int_\ell \boldsymbol{\Phi}^t \mathbf{f}_{ae}(x)\,\mathrm{d}x$ and $\mathbf{f}_{ae} = \frac{1}{2}\rho\left(V_m^{(k)}\right)^2 B\,\mathbf{c}_{ae}(\alpha)$
   ▷ extract from $\mu_R(\mathbf{w}^{(k)})$ the static rotation θ_{st} and compute $\alpha_m^{(k)} = \theta_{st}^{(k)} + \alpha_W$ (α_W mean wind inclination if present)
  Buffeting load: based on $\mathbf{w}^{(k)}$ (through $\mathbf{S}_\mathbf{v}(\omega)$), calculate $\mathbf{S}_{\tilde{P}}(\omega)$ with Eq. (11)
  $\overline{AD}$ **from APE:** define $f_\alpha(\alpha, \alpha_m^{(k)})$ via Eq. (15) and evaluate $\overline{AD}(V_r, \alpha_m^{(k)})$ with Eq. (14)
  Impedance matrix: with $\mathcal{M}$ and $\overline{AD}$ (through $\tilde{\mathbf{C}}_{se}$ and $\tilde{\mathbf{K}}_{se}$), calculate $\mathbf{E}_\eta(V_r, \omega)$ by Eq. (10)
  Stability check: with $\mathbf{E}_\eta$, check flutter stability and set $\mathrm{stable}(\mathbf{w}^{(k)}) \in \{\mathrm{true}, \mathrm{false}\}$
  Buffeting response: with $\mathbf{E}_\eta$ and $\mathbf{S}_{\tilde{P}}$, compute $\mathbf{S}_R(V_r, x, \omega)$ via Eq. (9)
   ▷ compute $m_{R_i}(\mathbf{w}^{(k)})$ with $i \in \{0, 1, 2\}$ via Eq. (3)
  Store outputs: $\left\{\mu_R(\mathbf{w}^{(k)}),\ \mathrm{stable}(\mathbf{w}^{(k)}),\ m_{R_i}(\mathbf{w}^{(k)})\right\}$
end for
for $h = 1$ **to** N_r **do**
  set $r = r^{(h)} \in \mathcal{R}$
  Upcrossing frequency: for each $\mathbf{w}^{(k)} \in \mathcal{W}$, use $\mu_R(\mathbf{w}^{(k)})$ and $m_{R_i}(\mathbf{w}^{(k)})$ to compute
   $\nu_R^+\!\left(r^{(h)} \,\middle|\, \mathbf{w}^{(k)}\right)$ with Eq. (2)
  Long-term response: using $\left\{\nu_R^+\!\left(r^{(h)} \,\middle|\, \mathbf{w}^{(k)}\right),\ \mathrm{stable}(\mathbf{w}^{(k)}),\ f_\mathbf{W}^{(k)}\right\}_{k=1}^{K}$, calculate
   $P\left[\hat{R}(T_{LT}) \le r^{(h)}\right]$ with Eq. (7)
   ▷ $\mathrm{stable}(\mathbf{w}^{(k)}) = \mathrm{false}$ implies $F_{\hat{R}(T)}(r^{(h)}|\mathbf{w}^{(k)}) = 0$
end for

Acknowledgments

The authors are grateful to Prof. Arvid Næss, a pioneer in extreme response and long-term analysis, for many insightful and instructive discussions about some of the topics of the current work.

Appendix A

To facilitate the application of the proposed methodology and the reproducibility of the results, Algorithm 1 specifies all the steps for the calculation of the long-term response of a bridge. Specifically, given $\mathbf{w}$ and accounting for the average parametric effect (APE), the short-term analysis yields the outputs $\left\{\mu_R(\mathbf{w}),\ \mathrm{stable}(\mathbf{w}),\ m_{R_i}(\mathbf{w})\right\}$. These stored quantities are then used for computing the annual non-exceedance probability of the bridge response as in Section 2.2.

Appendix B

Eq. (1) is based on the assumption of independent upcrossings and becomes asymptotically exact for very high thresholds (as $r \to \infty$, see Cramér 1966). However, long-span suspension bridges are lightly damped systems, whose dynamic response is largely governed by resonant components. This often leads to a narrow-banded response, especially as the system approaches flutter instability. Under such conditions, threshold crossings tend to occur in clusters, violating the assumption of statistical independence, even at relatively high threshold levels (see Crandall et al. 1966, Ditlevsen 1971). To this end, Vanmarcke (Vanmarcke, 1975) proposed an approximate formulation for a zero-mean stationary Gaussian process by modeling the envelope process through a two-state representation (below or above the threshold r) and introducing a correction based on the average clump size. This model has since been applied to a variety of problems (e.g., Vanmarcke and Lai 1980, Vanmarcke and Saunders 1985, Cacciola et al. 2004, Chen 2014). Here, we report the formulation for B-type crossings (i.e., one-sided thresholds), which is the only case easily extendable to processes with non-zero mean by simply considering the threshold $r - \mu_R$ for the associated zero-mean process:

$$F_{\hat{R}(T)}(r) = A(r)\exp\left[-\alpha_B(r)\cdot T\right] \tag{B.1}$$

where

$$A(r) = 1 - \exp\left[-\frac{(r-\mu_R)^2}{m_0}\right],$$
$$\alpha_B(r) = \nu_R^+(r)\cdot\frac{1-\exp\left[\sqrt{2\pi}\, q^{1.2}\,\frac{r-\mu_R}{\sqrt{m_0}}\right]}{1-\exp\left[\frac{r-\mu_R}{\sqrt{m_0}}\right]} \tag{B.2}$$

Here, $A(r)$ represents the probability that the process starts below the threshold r, and $\alpha_B(r)$ is the effective decay rate of the first crossing probability. The parameter ν_R^+ is the upcrossing rate for level r (as in Eq. (3)). The parameter $q = \sqrt{1 - m_{R_1}^2/(m_{R_0}\cdot m_{R_2})}$ (m_{Ri} are the spectral moments of the process) quantifies how the process is narrow-banded. It ranges between 0 and 1, with $q < 0.2$ typical for narrow-band processes. Following Vanmarcke (1975), an empirical exponent of 1.2 is used for q (to account for clusters of threshold crossings. The formulation for D-type crossings without mean can be found in Vanmarcke (1975).

For the present case study, α is computed for both B- and D-type crossings, excluding the static response, and results are shown in Fig. B.21. The qualitative trends reported in Fig. 1 of Vanmarcke (1975) are obtained, with the largest deviations from Rice theory occurring in the lateral response, which is characterized by the lowest values of q (approximately 0.4 for lateral and 0.5 for vertical and torsional response, considering a 100-years return period response threshold and wind scenario A). In the considered case, the typical value of $r/\sqrt{m_{R_0}}$ is around 3, which, according to Vanmarcke's formulation, can lead to a reduction up to 15% and 30% in the effective crossing frequency for the B- and D-crossing approach, respectively. However, these effects translate into small differences in probability and, consequently, in the response, amounting to about 1.5% and 6% at the 54% fractile of the response CDF if, for instance, a classical Davenport approach is used. The discrepancies decrease for higher fractiles. Moreover, for the present case study, the static response is significant for all components (and, this is always true for the lateral response), thus making only B-type crossing relevant and the impact of crossings' clustering negligible. Therefore, the additional complexity of including Vanmarcke's correction is not justified.

Appendix C. Supplementary data

The supplementary material includes raw and fitted aerodynamic data (e.g., 2D RFA surfaces), as well as bridge modal data.

Supplementary material related to this article can be found online at https://doi.org/10.1016/j.jweia.2026.106365.

Data availability

Data will be made available on request.

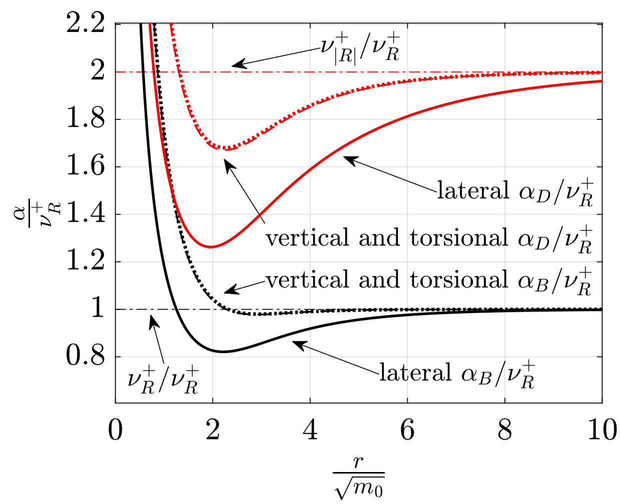

Fig. B.21. Ratio of Vanmarcke's probability decay rate to Rice's threshold crossing rate, calculated for the Halsafjorden Bridge for both B- and D-type barriers.

References

Aas-Jakobsen, K., Jamal, A., Tistel, J., 2023. Halsafjorden suspension bridge on floating foundation. Design and CO2 emission. In: IABSE Congress, New Delhi 2023: Engineering for Sustainable Development, Report. pp. 396–403. http://dx.doi.org/10.2749/newdelhi.2023.0396.

Agarwal, P., Manuel, L., 2009. Simulation of offshore wind turbine response for long-term extreme load prediction. Eng. Struct. 31 (10), 2236–2246. http://dx.doi.org/10.1016/j.engstruct.2009.04.002, URL: https://www.sciencedirect.com/science/article/pii/S0141029609001436.

Ágústsson, H., Furevik, B.R., Albretsen, J., 2024. Storms in Sulafjord- Wind, Waves and Currents. Technical Report METreport 03/2024, Norwegian Metereological Istitute, Oslo, Norway, Available online.

Argentini, T., Diana, G., Rocchi, D., Somaschini, C., 2016. A case-study of double multi-modal bridge flutter: Experimental result and numerical analysis. J. Wind Eng. Ind. Aerodyn. 151, 25–36.

ASCE-7-22, 2022. Minimum Design Loads and Associated Criteria for Buildings and Other Structures. American Society of Civil Engineers.

Baker, J.W., Cornell, C.A., 2003. Uncertainty Specification and Propagation for Loss Estimation Using FOSM Method. PEER Report 2003/07, Pacific Earthquake Engineering Research Center, College of Engineering, University of California, Berkeley.

Banday, Z.Z., Fenerci, A., Lystad, T.M., Øiseth, O.A., 2025. Buffeting induced fatigue damage assessment of long-span bridge decks under uncertain turbulence conditions. Eng. Struct. 323, 119292.

Barni, N., Bartoli, G., Mannini, C., 2024. Lyapunov stability of suspension bridges in turbulent flow. Nonlinear Dynam. 112 (19), 16711–16732.

Barni, N., Mannini, C., 2024. Parametric effects of turbulence on the flutter stability of suspension bridges. J. Wind Eng. Ind. Aerodyn. 245, 105615. http://dx.doi.org/10.1016/j.jweia.2023.105615, URL: https://www.sciencedirect.com/science/article/pii/S0167610523003173.

Barni, N., Øiseth, O.A., Mannini, C., 2021. Time-variant self-excited force model based on 2D rational function approximation. J. Wind Eng. Ind. Aerodyn. 211, 104523. http://dx.doi.org/10.1016/j.jweia.2021.104523, URL: https://www.sciencedirect.com/science/article/pii/S016761052100009X.

Barni, N., Øiseth, O.A., Mannini, C., 2022. Buffeting response of a suspension bridge based on the 2D rational function approximation model for self-excited forces. Eng. Struct. 261, 114267. http://dx.doi.org/10.1016/j.engstruct.2022.114267, URL: https://www.sciencedirect.com/science/article/pii/S0141029622003947.

Bocciolone, M., Cheli, F., Curami, A., Zasso, A., 1992. Wind measurements on the humber bridge and numerical simulations. J. Wind Eng. Ind. Aerodyn. 42 (1), 1393–1404. http://dx.doi.org/10.1016/0167-6105(92)90147-3, URL: https://www.sciencedirect.com/science/article/pii/0167610592901473.

Borgman, L.E., 1973. Probabilities for highest wave in hurricane. J. Waterw. Harb. Coast. Eng. Div. 99 (2), 185–207. http://dx.doi.org/10.1061/AWHCAR.0000184.

Bucher, C.G., Lin, Y.K., 1988. Stochastic stability of bridges considering coupled modes. J. Eng. Mech. ASCE 114 (12), 2055–2071. http://dx.doi.org/10.1061/(ASCE)0733-9399(1988)114:12(2055).

Buono, E., Katul, G., Heisel, M., Poggi, D., Peruzzi, C., Vettori, D., Manes, C., 2024. The vertical-velocity skewness in the atmospheric boundary layer without buoyancy and Coriolis effects. Phys. Fluids 36 (11).

Cacciola, P., Colajanni, P., Muscolino, G., 2004. Combination of modal responses consistent with seismic input representation. J. Struct. Eng. 130 (1), 47–55.

Calamelli, F., Rossi, R., Argentini, T., Rocchi, D., Diana, G., 2024. A nonlinear approach for the simulation of the buffeting response of long span bridges under non-synoptic storm winds. J. Wind Eng. Ind. Aerodyn. 247, 105681. http://dx.doi.org/10.1016/j.jweia.2024.105681, URL: https://www.sciencedirect.com/science/article/pii/S0167610524000448.

Castellon, D.F., Fenerci, A., Øiseth, O., 2022. Environmental contours for wind-resistant bridge design in complex terrain. J. Wind Eng. Ind. Aerodyn. 224, 104943. http://dx.doi.org/10.1016/j.jweia.2022.104943, URL: https://www.sciencedirect.com/science/article/pii/S0167610522000484.

Castellon, D.F., Fenerci, A., Petersen, Ø.W., Øiseth, O., 2023. Full long-term buffeting analysis of suspension bridges using Gaussian process surrogate modelling and importance sampling Monte Carlo simulations. Reliab. Eng. Syst. Saf. 235, 109211. http://dx.doi.org/10.1016/j.ress.2023.109211, URL: https://www.sciencedirect.com/science/article/pii/S0951832023001266.

Chen, X., 2014. Extreme value distribution and peak factor of crosswind response of flexible structures with nonlinear aeroelastic effect. J. Struct. Eng. 140 (12), 04014091.

Chen, X., Kareem, A., 2001. Nonlinear response analysis of long-span bridges under turbulent winds. J. Wind Eng. Ind. Aerodyn. 89 (14–15), 1335–1350.

Chen, X., Kareem, A., 2003. Aeroelastic analysis of bridges: effects of turbulence and aerodynamic nonlinearities. J. Eng. Mech. 129 (8), 885–895.

Chen, X., Matsumoto, M., Kareem, A., 2000. Aerodynamic coupling effects on flutter and buffeting of bridges. J. Eng. Mech. 126 (1), 17–26.

Ciampoli, M., Petrini, F., Augusti, G., 2011. Performance-based wind engineering: Towards a general procedure. Struct. Saf. 33 (6), 367–378.

Cook, N., Mayne, J., 1979. A novel working approach to the assessment of wind loads for equivalent static design. J. Wind Eng. Ind. Aerodyn. 4 (2), 149–164. http://dx.doi.org/10.1016/0167-6105(79)90043-6, URL: https://www.sciencedirect.com/science/article/pii/0167610579900436.

Cook, N., Mayne, J., 1980. A refined working approach to the assessment of wind loads for equivalent static design. J. Wind Eng. Ind. Aerodyn. 6 (1–2), 125–137.

da Costa, B.M., Wang, J., Jakobsen, J.B., Snæbjörnsson, J.T., Øiseth, O.A., 2023. Long-term response of a curved floating bridge to inhomogeneous wind fields. J. Wind Eng. Ind. Aerodyn. 240, 105488.

Cramér, H., 1966. On the intersections between the trajectories of a normal stationary stochastic process and a high level. Ark. Mat. 6 (4), 337–349.

Crandall, S.H., Chandiramani, K.L., Cook, R.G., 1966. Some first-passage problems in random vibration. J. Appl. Mech. 33 (3), 532–538. http://dx.doi.org/10.1115/1.3625118.

Davenport, A.G., 1961. The application of statistical concepts to the wind loading of structures. Proc. Inst. Civ. Eng. 19 (4), 449–472.

Davenport, A.G., 1962. Buffetting of a suspension bridge by storm winds. J. Struct. Div. 88 (3), 233–270.

Denoël, V., 2015. Multiple timescale spectral analysis. Probab. Eng. Mech. 39, 69–86. http://dx.doi.org/10.1016/j.probengmech.2014.12.003, URL: https://www.sciencedirect.com/science/article/pii/S0266892014400092.

Diana, G., Bruni, S., Cigada, A., Collina, A., 1993. Turbulence effect on flutter velocity in long span suspended bridges. J. Wind Eng. Ind. Aerodyn. 48, 329–342.

Diana, G., Fiammenghi, G., Belloli, M., Rocchi, D., 2013. Wind tunnel tests and numerical approach for long span bridges: The messina bridge. J. Wind Eng. Ind. Aerodyn. 122, 38–49. http://dx.doi.org/10.1016/j.jweia.2013.07.012, URL: https://www.sciencedirect.com/science/article/pii/S0167610513001578.

Diana, G., Omarini, S., 2020. A non-linear method to compute the buffeting response of a bridge validation of the model through wind tunnel tests. J. Wind Eng. Ind. Aerodyn. 201, 104163. http://dx.doi.org/10.1016/j.jweia.2020.104163, URL: https://www.sciencedirect.com/science/article/pii/S0167610520300738.

Diana, G., Resta, F., Rocchi, D., 2008. A new numerical approach to reproduce bridge aerodynamic non-linearities in time domain. J. Wind Eng. Ind. Aerodyn. 96 (10), 1871–1884. http://dx.doi.org/10.1016/j.jweia.2008.02.052, URL: https://www.sciencedirect.com/science/article/pii/S0167610508000561.

Ditlevsen, O., 1971. Extremes and First Passage Times with Applications in Civil Engineering (Ph.D. thesis). Technical University of Denmark.

Dunham, K.K., 2016. Coastal highway route E39 - Extreme crossings. Transp. Res. Procedia 14, 494–498. http://dx.doi.org/10.1016/j.trpro.2016.05.102, URL: https://www.sciencedirect.com/science/article/pii/S235214651630103X. Transport Research Arena TRA2016.

ENV1991-1-4, 2010. Eurocode 1: Actions on structures - part 1-4: General actions - wind actions.

Fenerci, A., Geuzaine, M., Denoël, V., Øiseth, O., 2022. Efficient long-term extreme response analysis of floating bridges using multiple timescale spectral analysis. In: International Conference on Offshore Mechanics and Arctic Engineering, vol. 85864, American Society of Mechanical Engineers, V002T02A026.

Fenerci, A., Øiseth, O., 2017a. The hardanger bridge monitoring project: Long-term monitoring results and implications on bridge design. Procedia Eng. 199, 3115–3120.

Fenerci, A., Øiseth, O., 2017b. Measured buffeting response of a long-span suspension bridge compared with numerical predictions based on design wind spectra. J. Struct. Eng. 143 (9), 04017131.

Fenerci, A., Øiseth, O., 2018. Strong wind characteristics and dynamic response of a long-span suspension bridge during a storm. J. Wind Eng. Ind. Aerodyn. 172, 116–138. http://dx.doi.org/10.1016/j.jweia.2017.10.030, URL: https://www.sciencedirect.com/science/article/pii/S016761051730541X.

Gao, G., Zhu, L., Øiseth, O.A., 2024. Nonlinear indicial functions for modelling aeroelastic forces of bluff bodies. Nonlinear Dynam. 112 (2), 811–832.

Gaspar, B., Teixeira, A., Soares, C.G., 2014. Assessment of the efficiency of kriging surrogate models for structural reliability analysis. Probab. Eng. Mech. 37, 24–34. http://dx.doi.org/10.1016/j.probengmech.2014.03.011, URL: https://www.sciencedirect.com/science/article/pii/S0266892014000253.

Giske, F.I.G., Leira, B.J., Øiseth, O., 2017. Full long-term extreme response analysis of marine structures using inverse FORM. Probab. Eng. Mech. 50, 1–8. http://dx.doi.org/10.1016/j.probengmech.2017.10.007, URL: https://www.sciencedirect.com/science/article/pii/S0266892017300760.

Gumbel, E., 1958. Statistics of Extremes. Columbia University Press, URL: https://books.google.it/books?id=JE1izgEACAAJ.

Haver, S., Kleiven, G., 2004. Environmental contour lines for design purposes: Why and when? In: Proceedings of the International Conference on Offshore Mechanics and Arctic Engineering. In: International Conference on Offshore Mechanics and Arctic Engineering, 23rd International Conference on Offshore Mechanics and Arctic Engineering, Volume 1, Parts A and B, pp. 337–345. http://dx.doi.org/10.1115/OMAE2004-51157.

Van der Hoven, I., 1957. Power spectrum of horizontal wind speed in the frequency range from 0.0007 to 900 cycles per hour. J. Atmospheric Sci. 14 (2), 160–164. http://dx.doi.org/10.1175/1520-0469(1957)014<0160:PSOHWS>2.0.CO;2, URL: https://journals.ametsoc.org/view/journals/atsc/14/2/1520-0469_1957_014_0160_psohws_2_0_co_2.xml.

Hu, Z., Mahadevan, S., 2016. A single-loop kriging surrogate modeling for time-dependent reliability analysis. J. Mech. Des. 138 (6), 061406. http://dx.doi.org/10.1115/1.4033428.

Jain, A., Jones, N.P., Scanlan, R.H., 1996. Coupled flutter and buffeting analysis of long-span bridges. J. Struct. Eng. ASCE 122 (7), 716–725. http://dx.doi.org/10.1061/(ASCE)0733-9445(1996)122:7(716).

Katsuchi, H., Jones, N.P., Scanlan, R.H., 1999. Multimode coupled flutter and buffeting analysis of the Akashi Kaikyo Bridge. J. Struct. Eng. ASCE 125 (1), 60–70. http://dx.doi.org/10.1061/(ASCE)0733-9445(1999)125:1(60).

Kleiven, G., Haver, S., 2004. Met-ocean contour lines for design; correction for omitted variability in the response process. In: Proceedings of the International Ocean and Polar Engineering Conference. In: International Ocean and Polar Engineering Conference, All Days, pp. 04–313.

Kopp, G.A., Morrison, M.J., 2018. Component and cladding wind loads for low-slope roofs on low-rise buildings. J. Struct. Eng. 144 (4), 04018019.

Krogstad, H.E., 1985. Height and period distributions of extreme waves. Appl. Ocean Res. 7 (3), 158–165. http://dx.doi.org/10.1016/0141-1187(85)90008-2, URL: https://www.sciencedirect.com/science/article/pii/0141118785900082.

Leadbetter, M., Lindgren, G., Rootzén, H., 1983. Extremes and related properties of random sequences and processes, first ed. Applied Probability Series, Springer, New York, http://dx.doi.org/10.1007/978-1-4899-3362-2.

Lei, S., Patruno, L., Mannini, C., de Miranda, S., Ge, Y., 2024. Time-domain state-space model formulation of motion-induced aerodynamic forces on bridge decks. J. Wind Eng. Ind. Aerodyn. 255, 105937. http://dx.doi.org/10.1016/j.jweia.2024.105937, URL: https://www.sciencedirect.com/science/article/pii/S0167610524003003.

Liu, L., Hu, F., Cheng, X.L., 2011. Probability density functions of turbulent velocity and temperature fluctuations in the unstable atmospheric surface layer. J. Geophys. Res.: Atmospheres 116 (D12), D12.

Lystad, T.M., Fenerci, A., Øiseth, O., 2020. Buffeting response of long-span bridges considering uncertain turbulence parameters using the environmental contour method. Eng. Struct. 213, 110575.

Lystad, T.M., Fenerci, A., Øiseth, O.A., 2021. Long-term extreme buffeting response of cable-supported bridges with uncertain turbulence parameters. Eng. Struct. 236, 112126.

Lystad, T.M., Fenerci, A., Øiseth, O., 2023. Full long-term extreme buffeting response calculations using sequential Gaussian process surrogate modeling. Eng. Struct. 292, 116495. http://dx.doi.org/10.1016/j.engstruct.2023.116495, URL: https://www.sciencedirect.com/science/article/pii/S0141029623009100.

Madsen, H., Krenk, S., Lind, N., 2006. Methods of Structural Safety. Dover Civil and Mechanical Engineering Series, Dover Publications, URL: https://books.google.it/books?id=e8sZjD7so-AC.

Melchers, R., Beck, A., 2018. Structural Reliability Analysis and Prediction. Wiley, URL: https://books.google.it/books?id=8yE6DwAAQBAJ.

Næss, A., 1984. On the long-term statistics of extremes. Appl. Ocean Res. 6 (4), 227–228.

Næss, A., Moan, T., 2013. Stochastic Dynamics of Marine Structures. Cambridge University Press.

Norwegian Technology Standards Institution, 2007. NORSOK standard N-003: Actions and action effects.

Øiseth, O., Rönnquist, A., Sigbjörnsson, R., 2010. Simplified prediction of wind-induced response and stability limit of slender long-span suspension bridges, based on modified quasi-steady theory: A case study. J. Wind Eng. Ind. Aerodyn. 98 (12), 730–741.

Pigolotti, L., Mannini, C., Bartoli, G., 2017. Experimental study on the flutter-induced motion of two-degree-of-freedom plates. J. Fluids Struct. 75, 77–98. http://dx.doi.org/10.1016/j.jfluidstructs.2017.07.014, URL: https://www.sciencedirect.com/science/article/pii/S0889974617300786.

Poirel, D., Price, S., 2003. Response probability structure of a structurally nonlinear fluttering airfoil in turbulent flow. Probab. Eng. Mech. 18 (2), 185–202. http://dx.doi.org/10.1016/S0266-8920(03)00013-4, URL: https://www.sciencedirect.com/science/article/pii/S0266892003000134.

Quintela, J., Montoya, M.C., Jurado, J.Á., Hernández, S., 2025. Reliability analysis and parametric studies of the buffeting performance of long-span bridges under multiple sets of random variables. J. Wind Eng. Ind. Aerodyn. 263, 106112.

Rasmussen, C.E., Williams, C.K.I., 2005. Gaussian Processes for Machine Learning. The MIT Press, http://dx.doi.org/10.7551/mitpress/3206.001.0001.

Rice, S., 1944. Mathematical analysis of random noise. Bell Syst. Tech. J. 23 (3), 282–332.

Sagrilo, L., Næss, A., Doria, A., 2011. On the long-term response of marine structures. Appl. Ocean Res. 33 (3), 208–214. http://dx.doi.org/10.1016/j.apor.2011.02.005, URL: https://www.sciencedirect.com/science/article/pii/S0141118711000204.

Salvatori, L., Spinelli, P., 2006. Effects of structural nonlinearity and along-span wind coherence on suspension bridge aerodynamics: Some numerical simulation results. J. Wind Eng. Ind. Aerodyn. 94 (5), 415–430.

Solari, G., 1997. Wind-excited response of structures with uncertain parameters. Probab. Eng. Mech. 12 (2), 75–87.

Vanmarcke, E.H., 1975. On the distribution of the first-passage time for normal stationary random processes. J. Appl. Mech. 42 (1), 215–220. http://dx.doi.org/10.1115/1.3423521.

Vanmarcke, E.H., Lai, S.S.P., 1980. Strong-motion duration and RMS amplitude of earthquake records. Bull. Seismol. Soc. Am. 70 (4), 1293–1307.

Vanmarcke, E., Saunders, H., 1985. Random fields: Analysis & synthesis. J. Vib. Acoust. Stress. Reliab. Des. 107 (2), 270–271. http://dx.doi.org/10.1115/1.3269255.

Winterstein, S.R., Ude, T.C., Cornell, C.A., Bjerager, P., Haver, S., 1993. Environmental parameters for extreme response: Inverse FORM with omission factors. In: Proceedings of the ICOSSAR-93. Innsbruck, Austria, pp. 551–557.

Wu, B., Shen, H., Liao, H., Wang, Q., Liu, J., 2023. Identification of amplitude-dependent damping ratio and flutter derivatives of a streamlined box girder under various wind angles of attack. J. Bridg. Eng. 28 (7), 04023041.

Wu, B., Wang, Q., Liao, H., Li, Y., Li, M., 2020. Flutter derivatives of a flat plate section and analysis of flutter instability at various wind angles of attack. J. Wind Eng. Ind. Aerodyn. 196, 104046. http://dx.doi.org/10.1016/j.jweia.2019.104046, URL: https://www.sciencedirect.com/science/article/pii/S0167610519306464.

Xiao, N.C., Zuo, M.J., Zhou, C., 2018. A new adaptive sequential sampling method to construct surrogate models for efficient reliability analysis. Reliab. Eng. Syst. Saf. 169, 330–338. http://dx.doi.org/10.1016/j.ress.2017.09.008, URL: https://www.sciencedirect.com/science/article/pii/S0951832016305312.

Xu, Z., Dai, G., Chen, Y.F., Rao, H., 2022. Prediction of long-term extreme response due to non-Gaussian wind on a HSR cable-stayed bridge by a hybrid approach. J. Wind Eng. Ind. Aerodyn. 231, 105217.

Xu, F., Yang, J., Zhang, M., Yu, H., 2021. Experimental investigations on post-flutter performance of a bridge deck sectional model using a novel testing device. J. Wind Eng. Ind. Aerodyn. 217, 104752.